Crowder and surface effects on self-organization of microtubules

Sumon Sahu [1], Lena Herbst [2], Ryan Quinn [3], and Jennifer L. Ross [1,*]

[1]*Department of Physics, Syracuse University, Syracuse, New York 13244, USA*

[2]*Department of Microbiology, University of Massachusetts Amherst, Amherst, Massachusetts 01003, USA*

[3]*Department of Biochemistry and Molecular Biology, University of Massachusetts Amherst, Amherst, Massachusetts 01003, USA*

(Received 13 September 2020; revised 5 May 2021; accepted 14 May 2021; published 16 June 2021)

Microtubules are an essential physical building block of cellular systems. They are organized using specific crosslinkers, motors, and influencers of nucleation and growth. With the addition of antiparallel crosslinkers, microtubule self-organization patterns go through a transition from fanlike structures to homogeneous tactoid condensates in vitro. Tactoids are reminiscent of biological mitotic spindles, the cell division machinery. To create these organizations, we previously used polymer crowding agents. Here we study how altering the properties of the crowders, such as type, size, and molecular weight, affects microtubule organization. Comparing simulations with experiments, we observe a scaling law associated with the fanlike patterns in the absence of crosslinkers. Tactoids formed in the presence of crosslinkers show variable length, depending on the crowders. We correlate the subtle differences to filament contour length changes, affected by nucleation and growth rate changes induced by the polymers in solution. Using quantitative image analysis, we deduce that the tactoids differ from traditional liquid crystal organization, as they are limited in width irrespective of crowders and surfaces, and behave as solidlike condensates.

DOI: 10.1103/PhysRevE.103.062408

I. INTRODUCTION

Cytoskeletal systems inside a cell, composed of actin, microtubules, and their associated proteins, are dynamic and complex in nature. The organization and rapid reorganization of cytoskeletal fibers are responsible for various crucial jobs in cells such as cell division, morphogenesis, and cell motility. One essential microtubule-based organization is the mitotic spindle. This dynamic, self-organized machine spontaneously forms around condensed and duplicated chromosomes in order to align and eventually separate the DNA into two daughter cells during cell division. The physics behind spindle formation, steady-state behavior, and transition into later stages of cell division is of primary interest to cell biology, biophysics, and soft condensed matter physics, as it could reveal important information to active matter physics [1].

The spindle shape and fluidity of the mitotic spindle are reminiscent of the tactoid liquid crystalline phase [2]. Since the spindle is made from microtubule filaments, which have a high aspect ratio, it is reasonable to apply liquid crystal models and theories. Tactoids are condensed phases of aligned liquid crystal molecules in a background of isotropic molecules. They can be bipolar or homogeneous, depending on the director field within the condensate. Bipolar tactoids have two point defects on the surface (boojums) at opposite ends, while homogeneous tactoids' defects exist at infinity, so that the director vector field is constant within the condensate. Liquid crystal theory has been used previously to explain the shape and director field inside tactoids [3,4]. The organization is a result of the interplay between the bulk elastic energy and anisotropic surface energy.

Tactoid organization has been observed in a variety of biological systems composed of elements with high aspect ratio, including actin [5–7], amyloid fibrils [8,9], tobacco mosaic viruses [10,11], and fd viruses [12,13]. Condensation of biological tactoids can be driven by specific crosslinking [5], macromolecular crowding [14], and high density of particles [6,15], which are passive, entropic drivers of self-assembly.

We have previously shown that microtubules can also condense into tactoids with the addition of a passive microtubule crosslinker, MAP65, a member of the MAP65/Ase1/PRC1 family used in spindle organization in plants, mammalian, and yeast cells [16]. This family of crosslinkers has been found in the mitotic spindle midzone in metaphase, telophase, and cytokinesis [17,18]. MAP65 binds specifically to antiparallel microtubule overlaps via a single microtubule-binding domain with a self-associating "crossbridge region" that is flexible, about 25 nm in length [19–21]. MAP65 binding is comparatively low affinity $K_D \sim 1.2\ \mu$M (low dwell time on microtubule) with contact angle dependent binding [22]. Interestingly, it has been shown that MAP65 promotes tubulin assembly, influencing nucleation by reducing the critical concentration of tubulin required for spontaneous filament nucleation [23,24]. In our prior work, we found that microtubule tactoids were homogeneous, nematic tactoids [16]. Unlike other biological tactoids or the mitotic spindle itself, our homogeneous microtubule tactoids were not able to coalesce or internally rearrange, as would be expected for a liquid [16], leading us to conclude that they were jammed. Another interesting observation was that these microtubule tactoids displayed a limited width.

*Corresponding author: jlross@syr.edu

Our prior work was performed in specific conditions, leading us to speculate that the jammed nature of the tactoids could be due to the experimental methods we used. Specifically, we used polymers in solution to aid in condensation and polymers on the surface of the experimental chamber to eliminate protein adhesion. We supposed that these large, complex polymers could alter the filament interactions to reduce mobility of the microtubule organizations.

In order to explore these possibilities, we quantify microtubule organization in the presence and absence of MAP65 with altered macromolecular crowding agents and surface treatments. We perform experiments as well as simulations to understand the mechanism of microtubule pattern formation and scaling associated with these patterns. Overall, we find that the microtubule contour length and the presence of the MAP65 have the largest effects on the organizations we observe. We find that the crowding agents have mild affects on patterns, most likely due to polymer effects on microtubule nucleation and growth, which affect microtubule contour length. The surface interaction is important in the absence of MAP65, when microtubules self-organize onto the surface, driven there by depletion interactions. These studies demonstrate the reproducibility of microtubule tactoids, which continue to be homogeneous and jammed with fixed width.

II. METHODS AND TECHNIQUES

A. Tubulin preparation

Unlabeled and fluorescently labeled (Dylight 488) lyophilized tubulin from porcine brain is purchased from Cytoskeleton. Tubulins are resuspended to 5 mg/ml in PEM-80 buffer (80 mM PIPES, pH 6.8, 1 mM $MgSO_4$, 1 mM EGTA). Fluorescent and unlabeled tubulin are combined to a final labeling ratio of ≈4% fluorescently labeled tubulin. Tubulin is aliquoted, drop frozen, and stored at −80 °C for later use. Aliquots are thawed on ice prior to use.

B. MAP65

The microtubule crosslinker MAP65-1 (MAP65) plasmid was a gift from Ram Dixit (Washington University, Saint Louis). The full protein purification protocol is detailed in [22,25]. Briefly, protein is expressed using *Escherichia coli* BL21(DE3) cells, grown to an OD_{600} of 1, lysed, and clarified. MAP65 protein is recovered from the lysate through affinity between the 6× histidine tag and Ni-binding substrate [25]. Purified protein is checked on an SDS-PAGE gel, aliquoted, and stored at −80 °C.

C. Crowding agents

Stock solutions of macromolecular crowders used for these experiments are dissolved in PEM-80 buffer or ddH_2O (water). The polymers we used are as follows: 8 kDa polyethylene glycol (8 kDa PEG), 14 kDa methylcellulose (14 kDa MC), 88 kDa methylcellulose (88 kDa MC), and 100 kDa polyethylene glycol (100 kDa PEG). Stock solutions of each polymer are as follows: 20% (w/v) 8 kDa PEG in PEM-80, 2.4% (w/v) 14 kDa MC in water, 3% (w/v) 88 kDa MC in water, and 5% (w/v) 100 kDa PEG in PEM-80. For experiments, outlined below, each of these stock solutions are diluted in the experimental mix to 1% (w/v) for 8 kDa PEG, 0.12% (w/v) for 14 kDa MC, 0.15% (w/v) for 88 kDa MC, and 0.25% (w/v) for 100 kDa PEG.

We selected to use these polymers because the PEG is a commonly used polymer in biological and soft matter systems as an inert crowder. It is a linear polymer that is highly studied so much is known about how the molecular weight scales with size and viscosity. The MC is a large, branched polymer used in food processing and gaining popularity in soft matter experiments as a crowder. Because we previously used this polymer in our last study [16], we wanted to continue to perform experiments with the original polymer as a control to ensure reproducibility.

The concentration of 88kDa MC is set because that was the amount we used previously, and we use this as our control parameter to ensure reproducibility and make comparisons to our prior work. For the current crowding agents, we seek to alter the molecular weight while maintaining the polymer in the dilute regime. Each polymer has a different critical concentration, c^*, that denotes the transition from dilute to semidilute regime. The concentrations we chose are to ensure that the polymers stayed in the same dilute regime, below their respective critical concentrations. After Tables I–III are given, the parameters of each polymer we used are reported in Table IV in Appendix A.

The second constraint is to have a lower viscosity due to the polymers in these experiments. The control 88 kDa MC has a measured viscosity of ≈2 cP, while we attempted to have the other crowders at a viscosity of ≈1 cP. We directly measured the kinematic viscosity of the polymer solutions as well as ddH_2O using an Ubbelohde glass capillary viscometer (Cannon Instrument) at 37 °C using a hot water bath. Kinematic viscosity (cSt) is multiplied by the density of the solutions (g/ml) to produce dynamic viscosity (cP) (viscosity used in this paper). The ddH_2O viscosity we measure at 37 °C was 0.77 cP. These viscosities are reported in Table IV in Appendix A.

D. Silanized coverslips

Coverslips are treated to inhibit protein binding to the surface using a block co-polymer brush of Pluronic-F127, as previously described [16]. Coverslips are cleaned with ethanol, acetone, potassium hydroxide (KOH) from Sigma, and treated with 2% (w/v) dimethyldichlorosilane solution (GE Healthcare) to make the surface hydrophobic. The full silanization protocol can be found in [26]. Just prior to use, these coverslips are coated with the block copolymer, Pluronic F127, to create a polymeric brush.

E. Lipid surface preparation

For samples with lipid bilayer surface coatings, we create small unilamellar vesicles (SUVs) to coat the surface. SUVs <100 nm in diameter are made of phospholipid 1-palmitoyl-2-oleoyl-glycero-3-phosphocholine (POPC) (Avanti) suspended in PEM-80 buffer. First, 40 μl of 10 mg/ml POPC in chloroform is well mixed with an additional 70 μl of chloroform. The lipid-chloroform mixture is

dried under N_2 gas and further desiccated inside a vacuum desiccator for >15 min. Dried lipid is resuspensed with PEM-80 buffer by using a vortex mixer for a minute to form giant unilamellar vesicles, which are sonicated for 3 min to form SUVs. The SUV solution is kept sealed with parafilm in 4 °C for use over one week. For experiments with labeled lipid bilayer surface, we use the same procedure with 1 mg/ml 18:1 Liss Rhod PE (Avanti) in chloroform.

F. Flow chamber preparation

Experimental flow chambers with an approximate volume of 10 μl are made from a cleaned glass slide (Fisher), glass coverslip (Fisher), and double-sided tape (3M). Glass slides are cleaned with 70% ethanol and water (milliQ) and dried using Kimwipes.

For samples with polymer surface coatings, silanized coverslips are used to create the chamber. The coverslip is coated with 5% Pluronic F127 by flowing into the chamber and incubating for 7–10 min in a humid environment to avoid evaporation. For samples with lipid bilayer coated surfaces, coverslips and slides are cleaned with Ultraviolet Ozone cleaner for 10 min prior to flowing in SUVs. Flow chambers are incubated in humid chambers to allow SUVs to adhere to the surface for ≈10 min. Chambers are washed with PEM-80 buffer to remove excess SUVs from solution.

After surface treatments are performed, the experimental assay mix (see below) is added, and chambers are sealed immediately afterwards with epoxy to prevent evaporation and flow in the sample. One chamber is used to inspect the experiment using fluorescence imaging (see below) while additional chambers are incubated at 37 °C for 1–3 h.

G. Experimental assay mix

The experimental assay mix contains tubulin, crowding agents, and crosslinkers as specified for each experiment. Each experimental assay mix contains 13.6 μM tubulin fluorescently labeled (4% labeling ratio), drop frozen, and thawed on ice. To enhance microtubule nucleation and stabilize microtubules, 1 mM GMPcPP (Jena Bioscience) is added. For experiments in polymer coated chambers, 0.5% F127 is added to maintain polymer surface coating. To limit photobleaching and photodamage during the experiment, 25 mM DTT is added with 0.25 mg/ml glucose oxidase, 0.075 mg/ml catalase from bovine liver, and 7.5 mg/ml glucose (all reagents from Sigma) as an oxygen scavenging system. Oxygen scavengers are added last, just prior to mixing and flowing into the chamber.

Specific crowders are added to the experimental mix as specified above. MAP65 crosslinkers are added to the solution, according to the percentage bound to tubulin: 0, 3, and 10%, which corresponds to 0, 0.44, and 1.49 μM final concentration [16].

We perform comparison experiments using the same reagents of proteins and chemicals in order to ensure reproducibility. Specifically, direct comparisons are made on the same week, using the exact same tubulin and MAP65 aliquots. This ensures the most direct comparison for different experiments.

H. Imaging

Imaging of microtubule organizations is performed using total internal reflection fluorescence (TIRF) microscopy on an inverted Nikon Ti-E microscope with Perfect Focus. The TIRF is illuminated using a 488-nm diode laser aligned into the epi-illumination path [26]. Image data are taken using a 60x oil-immersion (1.49 NA) objective, expanded with a 2.5x lens onto an Andor Ixon EM-CCD camera. The image scale is 108 nm per pixel. Images are displayed and recorded using the Nikon Elements software. Time series images are taken every 2 s for 1 h. Still images of chambers are imaged within 1–3 h.

Fluorescence recovery after photobleaching (FRAP) is performed using spinning disk microscopy (Yokogawa W1) on an inverted Nikon Ti-E microscope with Perfect Focus and 100x oil immersion (1.49 NA) objective imaged with a Andor Zyla CMOS camera. Confocal image acquisition and photobleaching were performed with a 561-nm laser and 405-nm laser with orthogonal stimulation, respectively. The data were taken as follows: (1) acquisition, 15 s with 2-s interval; (2) photobleaching, 5 s; (3) acquisition, 180 s with 2-s interval.

I. Turbidity measurements

Kinetics of tubulin polymerization in presence of crowding agents is quantified by absorbance measurements at $\lambda = 350$ nm, A_{350}. A flat bottom 96-well plate (Fisher) with experimental assay mix is placed in the microplate reader SpectraMax i3 (Molecular Devices) at 37 °C temperature to induce polymerization. Data are taken for 50 min in 45-s intervals. Each experimental configuration is performed in triplicate to check reproducibility of the results. We have six different experimental configurations: (1) the negative control sample, to normalize our data, contains PEM-80 buffer, DTT, oxygen scavenger, glucose, and tubulin with final concentration 13.6 μM but no nucleotide to initiate nucleation and growth of microtubules; (2) the positive control sample has the same reagents as the blank with GMPcPP added to induce microtubule polymerization; (3) experimental tests with same reagents as the positive control including (a) 1% (w/v) for 8 kDa PEG, (b) 0.12% (w/v) for 14 kDa MC, (c) 0.15% (w/v) for 88 kDa MC, and (d) 0.25% (w/v) for 100 kDa PEG.

Each curve is normalized to its average final and initial absorbance values and fit to the Boltzmann sigmoid equation [27]:

$$y = a - \frac{b}{1 + \exp\left(\frac{t - t_0}{\tau}\right)} \tag{1}$$

where a is the scaled final absorbance value ($a \sim 1$ after normalizing), b is the difference between scaled final and initial absorbance value ($b \sim 1$ after normalizing), t_0 is the inflection point, and τ is the characteristic time scale that signifies the flatness of the curve. The kinetics of the polymerization process can be captured in two parameters, the lag time for nucleation $t_{\text{lag}} = t_0 - 2\tau$ and the τ itself.

J. Data analysis

Self-organization of microtubules without crosslinkers is studied by orientation domain analysis using a FIJI plugin

called ORIENTATIONJ and further analyzed by custom MATLAB scripts, similar to prior methods [16]. First, raw gray scale images are smoothed two times in FIJI to reduce noise and pixelated regions. Next, we employ ORIENTATIONJ to the image to create a colored image map, where the color indicates the directionality of microtubules or microtubule bundles within the image. The settings used to create color maps are a 5×5 Gaussian window with cubic spline gradient scheme. Color saturation and brightness are kept constant. The color range [0, 255] of the resulting image map is equivalent to an angle range of $[0, \pi]$. In order to determine the size of domains pointing at similar angles, we use the color threshold command in FIJI to select regions in the following four color ranges: [0, 63], [64, 127], [128, 191], [192, 255]. The image map is turned into four individual orientation region maps by binarizing the color thresholded image maps. For each pixel (x, y) in the original image, the location is assigned to one of the four thresholded image maps and assigned a directionality index, $m = 1, 2, 3, 4$ corresponding to the four different directionality or color bins ([0, 63], [64, 127], [128, 191], [192, 255]).

The four m-type binary images are analyzed using moment analysis and spatial autocorrelation function analysis to determine the area parameters of the domains pointing in each direction. We use MATLAB's built-in analysis tool, region properties (REGIONPROPS), that returns the number and size of domains present in a binary image. We use definitions from percolation theory to describe our domains or clusters [28]. We define the domain size distribution as

$$n_s = \frac{\Lambda}{L^2} \tag{2}$$

where L is the size of our system or window size, and Λ is the number of domains with area s, within a window of size L^2. The values of L for experiment and CYTOSIM simulations are 55.3 and 50 μm, respectively, so this rescaling is used for comparisons. The average of n_s over all binary images produces $\overline{n}_s$, which is used to compare between different data sets.

The zeroth moment of the n_s distribution is the number of m-type domains in a binary image, defined as

$$N = \sum_{s=s_{\min}}^{s_{\max}} n_s. \tag{3}$$

The first moment of the n_s distribution defines the probability of m-type domains appearing in an image as

$$p = \sum_{s=s_{\min}}^{s_{\max}} s n_s. \tag{4}$$

Since we quantize our continuous rotation symmetry to four values, we should expect $p \sim 0.25$.

The average domain size $\langle s \rangle$ in an image of window size L^2 is defined by

$$\langle s \rangle = \frac{\sum_{s=s_{\min}}^{s_{\max}} s^2 n_s}{p}. \tag{5}$$

Here values of $s_{\min}$ and $s_{\max}$ are 1 and 2500 μm^2, respectively. The value of $s_{\min}$ is set by the binning size, which is 1 μm^2.

We can also compute the correlation length for the domain images using the binarized orientation images. The correlation length is found using the radially averaged pair autocorrelation function. Spatial autocorrelations can be calculated using fast Fourier transform (FFT) [29] according to the Weiner-Khinchin theorem:

$$G(\mathbf{r}) = \frac{F^{-1}(|F(I)|^2)}{\rho^2 M(\mathbf{r})} \tag{6}$$

where $F(I)$ is the FFT of a binarized image I, $|F(I)|^2$ is the power spectrum of the FFT of I, and $F^{-1}(I)$ is the inverse FFT of I. To avoid artifacts due to the periodic nature of the FFT, the images I are increased in size around the boundary by adding 200 additional pixels (experiment) or 300 pixels (cytosim) that are all set to zero (black) [30]. This additional number of pixels is chosen to be consistent with the rescaling.

In the denominator, ρ is the intensity per unit area in the image. Since the image is binarized, ρ exists between 0 and 1. $M(\mathbf{r}) = F^{-1}[|F(W)|^2]$, where W is the window function used for normalization as described in [30]. Specifically, W is an image of the same size as I (with padding) where all pixels are set to white (intensity equals 1). $G(\mathbf{r})$ is averaged in the azimuthal direction to give $\tilde{g}(r) = 1 + Ag(r)$, where A is the amplitude. For each binary image, $g(r)$ is fit with a sum of two exponentials $y(r) = ae^{-br} + ce^{-dr}$. In order to find a single correlation length, ξ, we determine the value of the radius where $y(\xi) = 0.37$, using the best fit equations. For each experimental parameter, $g(r)$ and ξ are averaged over several independent images to give $\overline{g}(r)$ and $\overline{\xi}$, respectively, which are used to compare between data sets.

Tactoid growth dynamics are analyzed using the MATLAB function REGIONPROPS on cropped binary images created using the Otsu global thresholding algorithm [31]. The area and major and minor axis lengths are determined for each frame and plotted over time. Intensity profiles along the major axis length are plotted to visualize the change over time. Each video is 1 h long and data were averaged over three tactoids.

Microtubule tactoids made in the presence of 10% MAP65 are imaged as still frames and analyzed in FIJI by hand to find the length and width. For comparison, we also use homemade MATLAB scripts using binarized images and the REGIONPROPS functions.

K. CYTOSIM

Agent based modeling is performed using an open source cytoskeletal filament simulating package, CYTOSIM [32]. Parameters used for the simulation are given in Table I. We choose the total filament length to represent the experimental concentration, which is controlled by the packing fraction ϕ [33]. The packing fraction is

$$\phi = \frac{2R_s}{L^2} l_{\text{total}} \tag{7}$$

where L is the window size in the simulation, R_s is the steric radius of the fiber, and l_{total} is the final total filament length. Filaments grow until the final total filament length l_{total} is exhausted and they reach a prescribed final mean filament length, l_c. Thus, the final total contour length $l_{\text{total}} = Nl_c$ is defined by the final mean filament length l_c and the number of

TABLE I. CYTOSIM parameters.

Simulation parameters	Values
Time step	0.1 s
Simulation time	1600 s
Viscosity	0.0025−2.5 N s/m^2[a,c,e]
Geometry (periodic)	50× 50 μm^2 (two-dimensional)
Packing fraction, ϕ	0.5, 0.75, 1
Rigidity	20 pN μm^2[a]
Initial growth speed, v_0	0.03 μm/s[c,d]
Catastrophe rate	0/s[c,e]
Growing force	1.7 pN[c]
Final total filament length, l_{total}	12 500, 18 750, 25 000 μm
Final mean filament length, l_c	2, 4, 6, 8 μm
Filament segmentation	1 μm[a,b,c]
Initial filament length	0.02 μm[b,c]
Steric radius, R_s	0.05 μm[a,b,c]
Steric force strength, k_s	50 pN/μm[c]
Depletion radius, R_d	0.03 μm[e]
Depletion force strength, k_d	50 pN/μm[a]

[a]Reference [35].
[b]Reference [33].
[c]Reference [34].
[d]Reference [38].
[e]This paper.

initial microtubule seeds, N. Filaments are allowed to grow from an initial length of 0.02 μm with an initial growing speed of 30 nm/s [34].

Because we are inspecting different polymers in the model, and these polymers create a depletion force, we wanted to implement a depletion force into the CYTOSIM modeling. The best method to do this would be to use a Derjaguin-like approximation for Asakura-Oosawa depletion forces. Unfortunately, CYTOSIM does not have this interaction type available. In order to mimic an effective depletion force, two prior papers [35,36] in the literature have used a piecewise function of repulsive and attractive springs with force, $F(r) = kr$, where r is the distance from the center of the filament. The spring constant depended on r as

$$k = \begin{cases} k_s, & \text{if } 0 \leqslant r \leqslant R_s \\ -k_d, & \text{if } R_s \leqslant r \leqslant R_s + R_d \\ 0, & \text{otherwise} \end{cases} \tag{8}$$

where k_s is purely repulsive within the steric radius R_s, and k_d is attractive between the range R_s and added depletion radius R_d to it.

Because this approximation is nonphysical, depletion forces do not increase with increasing distances, like the spring does, and we sought to check if this depletion interaction was necessary. We repeated the simulations without the attractive region of the piecewise function, with only the repulsive interaction. When we did this, we found only small effects on the quantitative numbers and no effects on the trends we observed. This is elaborated in Fig. 12, Appendix B.

Simulations are run long enough for the filaments to reach their prescribed final total filament length. Simulated filaments did not perform dynamic instability because we set the catastrophe rate to zero. This is done because experiments used GMPcPP, the slowly hydrolyzable analog of GTP, that virtually eliminates the catastrophe rate [37]. Since dynamic instability is blocked in our simulation, filaments only grow and the growth curve flattens as they reach steady state using this relationship:

$$v_i = v_0\left(1 - \frac{l_{\text{total},i}}{l_{\text{total}}}\right) \tag{9}$$

where v_i is the instantaneous growth speed; v_0 is the initial growth speed, listed in Table I; $l_{\text{total},i}$ is the instantaneous total filament length in the simulation; and l_{total} is the final total filament length of the simulation, as described above. All simulations are run for 1600 s to allow the system to reach steady state. The last frame is rendered as an image for analysis identical to that performed for experimental images.

III. RESULTS AND DISCUSSION

We seek to understand how the self-organization of microtubules depends on nonspecific forces from depletion agents and specific interactions via diffusible crosslinkers. Both mechanisms are responsible for minimizing the microtubule overlap area by contributing to the lateral interaction between them. As we demonstrated previously [16], nucleating and polymerizing microtubules resulted in microtubule self-organizations that showed a transition from fanlike domain patterns to elongated homogeneous tactoids as a function of MAP65 crosslinker concentration. These prior experiments used methylcellulose polymer as a crowder and a polymer-coated surface, which could have affected the organized patterns we observed. The tactoid phase was different from other biological tactoids in two ways: the width of the tactoids was constant and the microtubules inside the tactoids were jammed.

In order to determine the mechanism driving the pattern formation we previously observed, we have altered the crowding agent type, size, and molecular weight. Qualitatively, for polymer-coated surfaces, all crowders show a similar phase transition, from fanlike structures to tactoids (Fig. 1).

To test the effect of the surface on microtubule patterns, we repeat the experiments for 0 and 10% MAP65 in the presence of 88 kDa MC on a lipid-coated surface. The lipid surface is a fluid bilayer with a slip condition. Qualitatively, we observe that the lipid surface retains the fanlike pattern with increased disorder in the absence of MAP65. Tactoids form robustly on lipid surfaces (Fig. 2).

In an attempt to understand the mechanisms driving the patterns we observe, we simulate the microtubule growth and self-organization using the CYTOSIM software package (Fig. 3). Simulations allow us to alter the viscosity, depletion interactions, filament length, and growth rates independently and examine the dynamics to steady state.

A. Microtubule organization without crosslinkers

1. Polymer surface with different crowders

Qualitatively, fanlike surface patterns in the absence of crosslinkers are similar for different crowding agents (Fig. 1). To quantify the patterns of microtubule self-organization, we perform a domain analysis similar to our prior publication

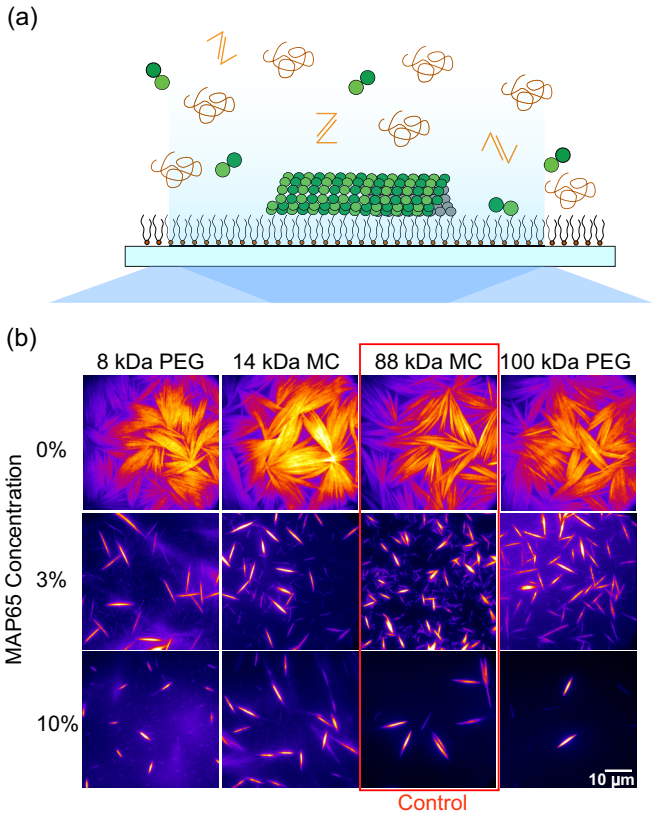

FIG. 1. (a) Schematic of the experimental system: Tubulin dimers (green) polymerize into microtubules in the presence of crowders (brown polymer balls) and crosslinkers (orange Z) on polymer-coated surfaces imaged with TIRF illumination. (b) Images showing microtubule patterns on polymer brush coated surfaces in the presence of crowders with different molecular weights (8 kDa PEG, 14 kDa MC, 88 kDa MC, 100 kDa PEG) with tubulin concentration 13.6 μM and MAP65 at 0% (top), 3% (middle), and 10% (bottom). Fanlike patterns were observed without MAP65 (top row). High MAP65, 10%, induced tactoidlike condensates (bottom row). The red box indicates 88 kDa MC, the condition used in our prior work, and serves as our reproducibility control state [16]. The scale bar is 10 μm for all images.

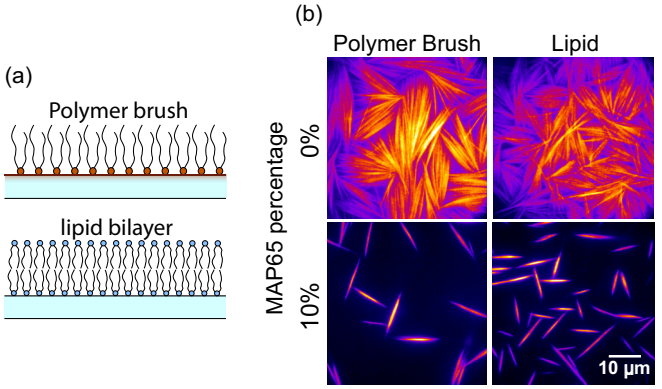

FIG. 2. Surface effects on patterns. (a) Schematic diagram of the F127 polymer brush surface (top) and lipid bilayer surface (bottom). (b) Images of microtubule organizations on polymer-brush surfaces (left column) and lipid surfaces (right column) in the presence of 0% MAP65 (top row) and 10% MAP65 (bottom row). The scale bar is 10 μm for all images.

[16], where the direction of locally oriented microtubule bundles in the pattern was identified automatically using the ORIENTATIONJ plugin in FIJI/IMAGEJ [Fig. 4(a-i)]. The image is colored according to the local orientation [Fig. 4(a-ii)] and that color map is used to identify domains where the angles are similar [Fig. 4(a-iii)]. We threshold the colors to a specific range of colors divided into four different bins that we identify with an index, m [Fig. 4(a-iv)]. The color or angle thresholding is used to create a binary image where the selected angle range is portrayed in white, and all other angle orientations are in black [Fig. 4(a-v)]. For each original image of microtubule patterns, we create four binary images highlighting one of the four angle ranges ($m = 1, 2, 3, 4$). We use the binary images to quantify the domain parameters of the images. Domain parameters of interest included the following: average domain size (s) distributions $\overline{n}_s$ [Fig. 4(b)] used to determine the average domain size $\overline{\langle s \rangle}$ and the radially averaged spatial mean autocorrelation function $\overline{g}(r)$ [Fig. 4(c)] that allows us to determine the mean correlation length $\overline{\xi}$ of the images.

Similar to our prior study, we first perform microtubule self-organization experiments using polymer-coated surfaces with four different crowding agents. We find that the average distributions of the domain areas (divided by the window size L^2 in order to compare with simulations) are all power laws [Fig. 4(b-i)]. We test the distributions using the Kolmogorov-Smirnov statistical test (KS test) and found that distribution for 8 kDa MC is significantly distinct from the rest of the distributions, rejecting the null hypothesis at the 5% significance level. We find 14 kDa MC and 100 kDa PEG data to be statistically similar (Appendix C, Table V). When we compare the average domain sizes for these images, the averages are different from one another, although they have large error bars due to "critical-domain"-like behavior that results in the power law (Table II).

In our prior work, we measured the area distributions for one crowder type, 88 kDa MC, and changed the contour length of the filaments by altering the tubulin concentration. Microtubule contour length was varied by changing the tubulin concentration, [TUB], as described in [16]. For, [TUB] = 13.6, 54.5, and 70 μM median contour lengths were 6.25, 2.5, and 1.1 μm, respectively. The more detailed analysis we are doing here was not performed for the prior experimental results. In order to compare our current experimental and simulation results to our prior results, we reanalyze our prior data [Fig. 4(b-ii)] [16]. The KS tests show that the area distributions are distinct from one another, rejecting the null hypothesis at the 5% significance level (Appendix C, Table VI). As reported previously, the average domain size decreases with increasing tubulin concentration (decreasing contour length) (Table II) [16].

Our previous experimental data suggest that the contour length of the microtubule filaments is the control parameter for the domain sizes we observe for microtubule self-organization on polymer coated surfaces without crosslinkers. Unfortunately, in the experiments, we had to increase the tubulin concentration in order to decrease the contour length, which also resulted in a higher number of filaments. Thus, the experiments lacked separate control over the contour length

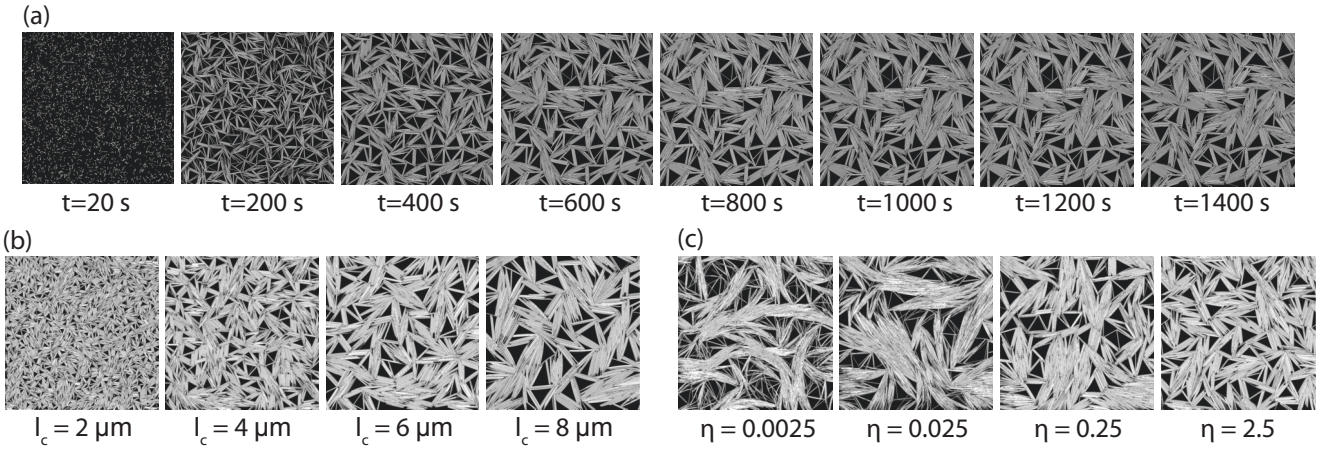

FIG. 3. CYTOSIM simulations of microtubule organization without crosslinkers. (a) Time series of fanlike microtubule pattern growth for parameters, $\phi = 0.75$, $\eta = 2.5$ Pa s, $l_c = 6$ μm with steric interaction and depletion forces present. Filaments grow from initial small seeds until they exhaust the total filament length. (b) The effect of l_c on patterns from left to right: $l_c = 2, 4, 6, 8$ μm with viscosity $\eta = 2.5$ Pa s and $\phi = 0.75$. (c) The effect of viscosity on steady-state patterns from left to right: $\eta = 0.0025,\ 0.025,\ 0.25,\ 2.5$ Pa s with $\phi = 0.75$, $l_c = 6$ μm. Final state patterns obtained at higher viscosities match experimental patterns qualitatively.

and the number of filaments. In order to directly test the mechanism that contour length is the control parameter for our prior results, here we use CYTOSIM to simulate polymerizing microtubules with a fixed total number of filaments and final microtubule contour length using the parameters described in the methods and described by prior published works (Table I) [33–35]. We plot the domain size distribution as shown in Fig. 4(b-iii). Examining the average domain size, we recapitulate the dependence on contour length, such that longer contour lengths result in larger average domain sizes (Table II). The KS test results show that contour lengths of 2 and 4 μm are distinct from all other distributions, but 6 and 8 μm data are statistically similar, using a 5% significance level to reject the null hypothesis (Appendix C, Table VII). Thus, our simulation agrees with our initial interpretation that the contour length is the likely control parameter for the domain area for orientational domains self-organized on the polymer-coated surfaces.

We find that the experimental and several of the simulated domain area distributions display a power law dependence.

TABLE II. Fanlike pattern data characteristics.

	Configuration	$\overline{\langle s \rangle}$ (μm^2) mean ± SD	$\overline{\xi}$ (μm) mean ± SD
	8 kDa PEG	217.8 ± 144.7	4.2 ± 1.4
[TUB]	14 kDa MC	245.7 ± 163.9	4.3 ± 1.5
= 13.6 μM	88 kDa MC	294.4 ± 195.0	5.0 ± 2.0
	100 kDa PEG	208.4 ± 129.9	3.9 ± 0.9
	13.6 μM	294.4 ± 195.0	5.0 ± 2.0
88 kDa	54.5 μM	134.0 ± 72.7	2.7 ± 0.3
MC	70 μM	93.3 ± 51.8	2.1 ± 0.5
	2 μm	37.3 ± 12.5	1.2 ± 0.1
$\phi = 0.75$	4 μm	60.5 ± 23.2	1.7 ± 0.2
	6 μm	108.3 ± 74.3	2.4 ± 0.3
	8 μm	132.4 ± 65.8	2.8 ± 0.5

In critical phenomena theory, power law behavior is achieved when a system approaches a critical point. Our data indicate there is a regime shift for the smallest contour length in simulation data, which did not display a power law. In this case, the distribution starts with a power law, then falls off exponentially, indicating a cutoff cluster size is present in the system. Conversely, configurations which contained large domain areas retain the power law behavior, a signature of critical phenomena. In literature it has been shown that the critical behavior of larger domains results from the finite size of the viewing window [28], and this is likely a factor here.

In order to further characterize the self-organization pattern for microtubules in the absence of crosslinkers, we characterize a different intrinsic length parameter, the correlation length, ξ. Using the same binarized images for each orientation domain, we determine the spatial autocorrelation function. Averaging over the different color images, we obtain $\overline{g}(r)$, and plot as a function of the radius from the center of the image [Fig. 4(c-i)]. This correlation length, ξ, is determined from each autocorrelation function, as described in the methods. These values are averaged over all binary images to define the mean correlation length $\overline{\xi}$ for each experimental parameter [Fig. 4(c-i), inset]. When we perform the KS test on the distribution of the correlation lengths, ξ, we find that the data are not statistically distinct for 8 kDa PEG, 14 kDa MC, and 100 kDa PEG, but the 88 kDa MC ξ values are statistically different from the rest (Appendix C, Table VIII).

In our previous study, we did not perform the correlation length analysis [16], so we seek to determine if this technique agrees with the domain size analysis. As with the domain analysis [Fig. 4(b-ii)], the autocorrelation function [Fig. 4(c-ii)] and correlation lengths [Fig. 4(c-ii), inset] appear to depend on the tubulin concentration (Table II). Indeed, the KS test results from correlation length distributions show that all the data are statistically distinct from one another (Appendix C, Table IX).

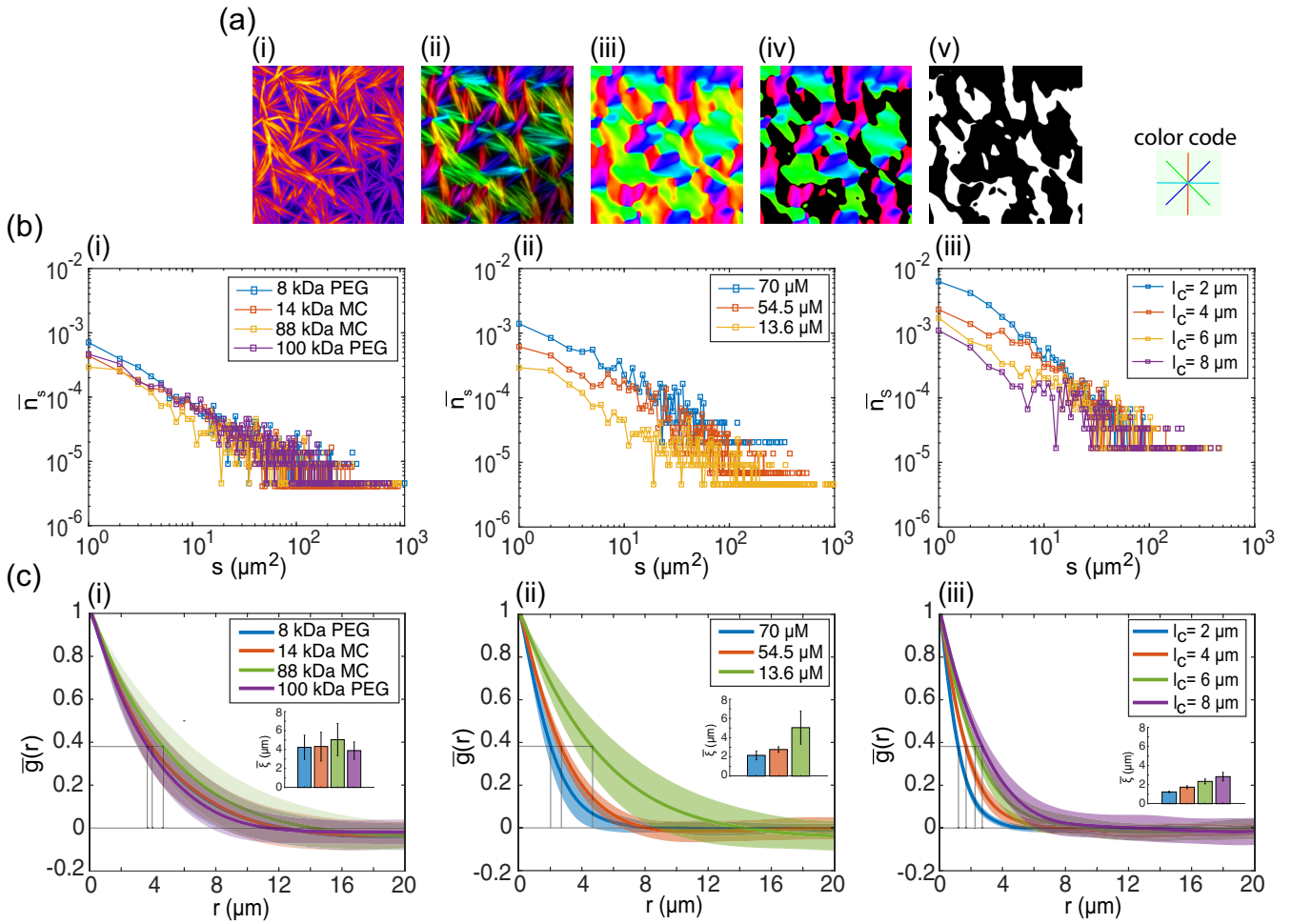

FIG. 4. (a) Orientation analysis. (a-i) Raw gray scale image with fire look up table. (a-ii) Image color coded according to orientation of fibers shown. (a-iii) Color coded regions. (a-iv) Selected orientation domain shown in black. (a-v) Binary image created with all regions of same color in white and other regions in black. (b) Average domain size distribution $\overline{n}_s$. (b-i) Different crowders with 13.6 μM tubulin ($n \geqslant 18$) for 8 kDa PEG (blue squares), 14 kDa MC (red squares), 88 kD MC (yellow squares), and 100 kDa PEG (purple squares). (b-ii) Different concentrations of tubulin with the MC 88 kDa crowder ($n \geqslant 4$) for 70 μM (blue squares), 54.5 μM (red squares), and 13.6 μM (yellow squares). Raw data from [16]. (b-iii) CYTOSIM simulation with four different contour lengths for $\phi = 0.75$ ($n = 6$) l_c is 2 μm (blue squares), 4 μm (red squares), 6 μm (yellow squares), and 8 μm (purple squares). (c) Radially averaged mean autocorrelation function, $g(r)$ plots. Lines represent average over all data, $\overline{g}(r)$, and the shaded region represents standard deviation of that average. (c-i) Different crowders with 13.6 μM tubulin ($n \geqslant 18$) for 8 kDa PEG (blue line), 14 kDa MC (red lines), 88 kD MC (green line), and 100 kDa PEG (purple lines). Inset data show the mean correlation length $\overline{\xi}$ with standard deviation (error bars) for 8 kDa PEG (blue bar), 14 kDa MC (red bar), 88 kD MC (green bar), and 100 kDa PEG (purple bar). (c-ii) Different concentrations of tubulin with the MC 88 kDa crowder ($n \geqslant 4$) for 70 μM (blue line), 54.5 μM (red line), and 13.6 μM (green line). Original raw data from [16]. Inset data show the mean correlation length $\overline{\xi}$ with standard deviation (error bars) for 70 μM (blue bar), 54.5 μM (red bar), and 13.6 μM (green bar). (c-iii) CYTOSIM simulation with four different contour lengths for $\phi = 0.75$ ($n = 6$) l_c is 2 μm (blue line), 4 μm (red line), 6 μm (yellow line), and 8 μm (purple line). Inset data show the mean correlation length $\overline{\xi}$ with standard deviation (error bars) for l_c is 2 μm (blue bar), 4 μm (red bar), 6 μm (yellow bar), and 8 μm (purple bar).

We perform the correlation length analysis on the simulated microtubule organizations. We find that the autocorrelation profiles $\overline{g}(r)$ and the mean correlation length $\overline{\xi}$ depend on the filament contour length [Table II, Fig. 4(c-iii)]. The simulation shows the same trend observed in experiments, and the KS test results on correlation length distributions show that they are all statistically distinct from one another [Appendix C, Table X, Fig. 4(c-iii) inset]. As above, these results provide added evidence that the contour length is likely the control parameter for the size of the patterns observed in the absence of the crosslinkers.

Both the domain area analysis and the autocorrelation analysis demonstrate that the contour length of the filaments is the most likely order parameter for the patterns we observe. The evidence for this conclusion is stronger when using the autocorrelation lengths, as the errorbars are comparatively smaller. As described above, the power law distribution for the domain areas likely emanates from the cutoff size due to the limited imaging and simulation areas that restrict the domain areas we can measure. For future studies, imaging and simulating over larger areas will allow more accurate measurement of large domains.

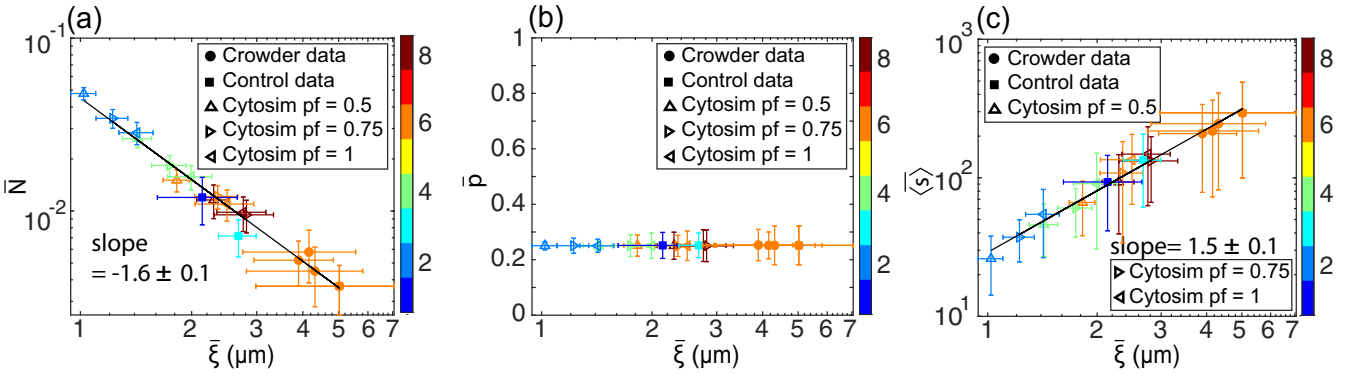

FIG. 5. (a) Average number of m-type ($m = 1, 2, 3, 4$) domains per image $\overline{N}$ plotted over mean correlation length $\overline{\xi}$ in log-log scale. (b) Mean probability of the m-type cluster present in an image $\overline{p}$ plotted as a function of $\overline{\xi}$ in semilog scale. (c) Average cluster size $\overline{\langle s \rangle}$ as a function of $\overline{\xi}$ in log-log scale. The color bar on the right corresponds to the median microtubule length expected for these data sets, as reported before in [16].

We can quantify the first three moments of n_s for the current experimental data, our prior experimental data [16], and current simulated data to compare them. The zeroth moment is the average number of m-type domains $\overline{N}$, the first moment is the mean probability that a position is in one of the four m-type domains $\overline{p}$, and the second moment is the average domain size $\overline{\langle s \rangle}$. We plot each as a function of mean correlation length, $\overline{\xi}$, our independent measure for the images (Fig. 5).

The number of domains (zeroth moment) shows a power law dependence on the mean correlation length with an exponent -1.6 ± 0.1 [Fig. 5(a), Appendix C, Table XI]. It is interesting to note that this dependence is preserved for the simulated data as well. For each data set, the expected contour length of the filaments is also displayed using a color-coded map. The contour-length color coding shows that the filament length is correlated, with longer contour lengths more likely in the longer correlation lengths and fewer, larger domains. The dependence is not as strongly correlated as the measured mean correlation length $\overline{\xi}$.

The probability of an m-type domain appearing in an image (first moment) is constant, $\overline{p} \sim 0.25$, no matter the contour length or correlation length [Fig. 5(b)]. As described in the methods, this is expected, since the images were binned into four orientation directions for analysis. If the local orientation of the domain is randomly determined and independent from its neighboring domain, we would expect the probability for the four orientation bins to be $\approx$0.25. This is a good check on our moments analysis, and confirms that the local orientational order is random and globally isotropic.

The average domain size (second moment) $\overline{\langle s \rangle}$ scales with the mean correlation length $\overline{\xi}$ with exponent 1.5 ± 0.1 [Fig. 5(c), Appendix C, Table XI]. The simulation data again fit into this relationship with the experimental data. Using the color coding for the contour length again shows the underlying dependence, as we observed for the zeroth moment. The magnitudes of the values for the power law of the average number of clusters and the average cluster size are the same, within the uncertainty of the fit. This is reasonable, since we place each pixel into a cluster, so the clusters are space filling in this analysis. This also serves as a check on our analysis methods.

Overall, the results indicate that filament length is the most likely underlying control parameter for the surface patterns that we observe. For the data with different crowding agents, we observe only modest differences between the crowders. There are three possible roles played by the crowders in our experiments. First, crowders induce bundling through the depletion interaction and exert compaction force to other filaments. Second, patterns are likely determined by the interaction with the surface, which can be affected by the depletion interaction with filaments and the surface. Indeed, the crowding agent is necessary for any patterns to form on the surface. Third, crowders could influence nucleation and tubulin assembly in initial stages, which would control the average microtubule number N and contour length l_c. Given the simulation results, we anticipate that this last mechanism is likely the cause for the subtle differences we observe for the average domain size (Figs. 4 and 5, Table II).

2. Turbidity measurements for different crowders

Our data beg the question: are the subtle differences we observe for different crowders due to the polymers altering the nucleation and growth kinetics to result in slightly different final contour lengths? We cannot directly determine the contour lengths for microtubules in the presence of these crowders using the microscope because the polymers also cause bundling. Prior experiments on tubulin nucleation and growth used a turbidity method and showed that the formation of microtubules was proportional to the PEG concentration for a fixed molecular weight of PEG molecules [39]. Specifically, higher concentrations of PEG increased the microtubule association constant, K_a, a determinant of microtubule growth, and reduced the lag time for nucleation. A second study showed that the K_a also increased as the PEG size increased [40].

We notice that the correlation lengths and the average domain sizes appear to be higher for MC molecules than for PEG molecules (Fig. 4, Table II). This would imply that PEG molecules could be better at enhancing nucleation and growth of microtubules than MC polymers at the concentrations we use in our paper. To directly quantify how the specific crowders we used in this paper can affect tubulin nucleation and

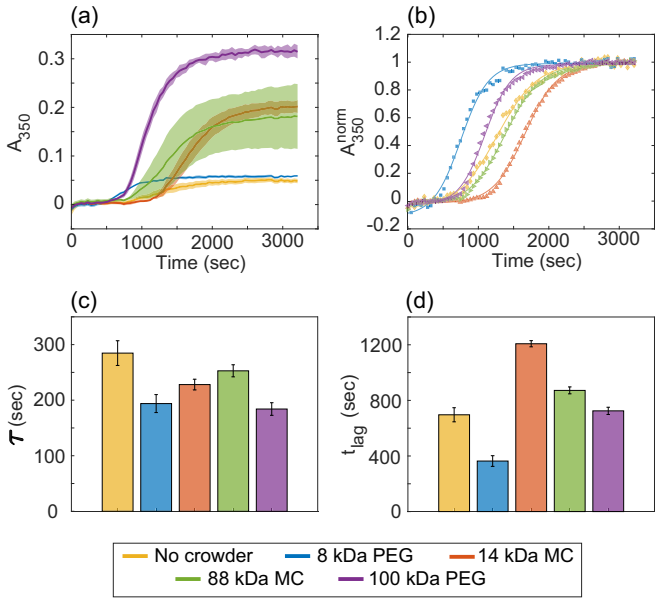

FIG. 6. Kinetics of polymerization for 13.6 μM tubulin. (a) Absorbance A_{350} data plotted vs time for no crowder (yellow), 8 kDa PEG (blue), 14 kDa MC (orange), 88 kDa MC (green), and 100 kDa PEG (magenta) with same polymer concentrations used in pattern formation experiments. The shaded regions are the standard deviation resulting from three independent measurements for each configuration ($n = 3$) using MATLAB [41]. (b) Normalized absorbance data plotted vs time for no crowder (yellow diamonds), 8 kDa PEG (blue squares), 14 kDa MC (orange upright triangles), 88 kDa MC (green, right pointing triangles), and 100 kDa PEG (magenta left pointing triangles) and fit with the Boltzmann sigmoid equation [Eq. (1), displayed as same color lines] (Appendix C, Table XII). (c) Characteristic time τ is shown in bar plot for the given configurations. Error bars represent 95% confidence interval for the fit parameter. (d) Lag time $t_{\rm lag}$, calculated from τ, shown as bar plot for each configuration. Error bars calculated from 95% confidence interval from the fit.

growth, we perform kinetic growth studies over time using turbidity. First, we compare the raw data without normalization and find that the maximum scattering depends on the crowding agent used [Fig. 6(a)]. Typically, the maximum turbidity signal would correlate to the total polymer mass, but there is likely enhanced scattering due to bundling in addition to the increased polymer mass.

In order to quantify the nucleation and growth time scales in these data, we normalize the data to start at zero and become maximum at 1. We fit the normalized data with a Boltzmann sigmoid equation (1) [Fig. 6(b)]. From the fit parameters (Appendix C, Table XII) we find the characteristic timescale for growth, τ, varies with crowders [Fig. 6(c)]. If τ is small, starting from nascent oligomers it takes less time to polymerize filaments, which will generate more microtubules of shorter length on average. Interestingly, we see the same pattern for the characteristic growth time that we observe and for the correlation length in the inset of Fig. 4(c-i). The similarities between these different data imply that the crowders could be changing the nucleation and growth kinetics, resulting in the modest pattern changes we observe.

From the turbidity data, we can also quantify the lag time for nucleation [Fig. 6(d)]. It appears that the PEG molecules, specifically the 8 kDa PEG, help enhance nucleation while the MC polymers inhibit nucleation. That is an interesting and unexpected result, since macromolecular crowding is expected to help bring objects together in general. One biochemical difference between PEG and MC is that MC is charged. It is perhaps this charge that could be causing interactions with the tubulin dimers to interfere with binding. Future, systematic experiments exploring different polymers with various charges, molecular weights, and concentrations may reveal more information about how polymer characteristics affect microtubule nucleation and growth.

3. *Lipid surfaces with different crowders*

Because crowding agents cause the depletion of microtubules onto the surface, we wanted to test the effects of the surface coating on microtubule self-organization in the absence of crosslinkers. We replace the polymer brush surface with a lipid bilayer surface to test the surface effects. We are able to recapitulate qualitative fanlike structures on the lipid surface [Fig. 2(b)], although the patterns are not as reproducible as those observed on polymer surfaces. More often, we observe bundles that overlap and are less locally aligned in the presence of the lipid bilayer [Fig. 7(a)]. Indeed, these patterns appear to be isotropic arrangements of bundles, not fanlike organizations.

We directly observe microtubules nucleating and growing on the surface to determine why the patterns are different [Fig. 7(b)]. When we examine the dynamics of the microtubules forming on the lipid bilayer surfaces, we often observe that in the initial stage microtubules do not show translation and rotational motion. They grow with time, keeping their orientation fixed to overlap or cross over each other to make the pattern less aligned. This is surprising, since the lipid bilayer should behave like a two-dimensional (2D) fluid. We monitored the fluidity of the lipid bilayer using fluorescence recovery after photobleaching on a fluorescent lipid bilayer [Fig. 7(c)]. We see recovery of the lipid fluorescence, as expected for a fluid surface. It is possible that the lack of mobility can be due to the interaction with the lipid surface, disrupted depletion giving access to z dimension. The patterns do not depend on the crowding agent used. So, the interaction between microtubules and the surface plays a role in determining whether fanlike structures could be formed and appears to be more influential than the specific crowding agent.

To attempt to understand the mechanisms that control the patterns on lipid bilayer surfaces, we perform simulations using CYTOSIM. Our experimental system is quasi-2D due to crowders, so we limit our CYTOSIM simulation space to 2D plus steric interactions (2D+S) [33]. As shown in Table IV the viscosity (dynamic) of the polymer solutions is $\approx$ 0–3 cP (mPa s) in our experiments. In the simulations we varied the viscosity from 0.0025 to 2.5 Pa s to determine if the surface effects act as a viscosity parameter [Fig. 3(c)].

Although CYTOSIM is able to achieve similar fanlike patterns at higher viscosity values [Fig. 3(a)], the dynamics of the pattern formation to reach steady state are distinct from what we observe in experiments. The CYTOSIM viscosity value

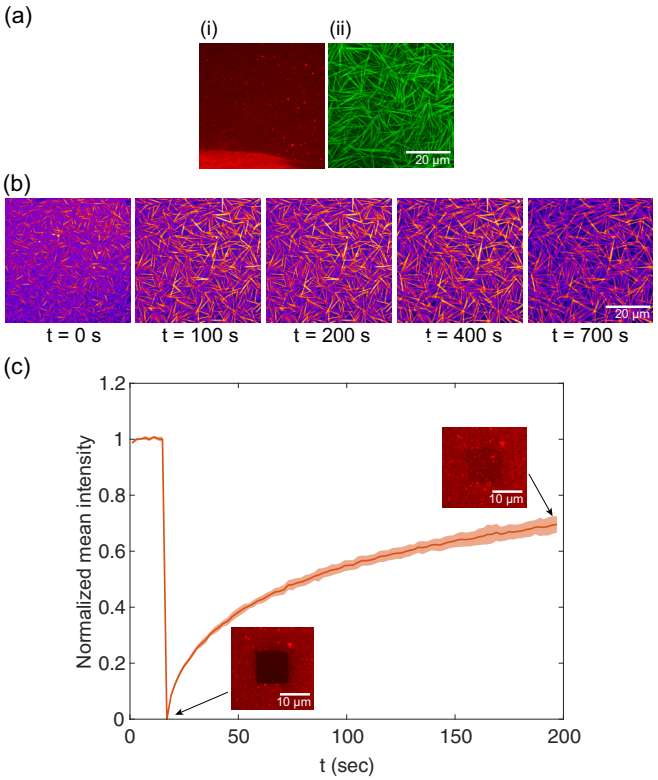

FIG. 7. (a) Two color image showing the lipid bilayer (561 nm, red) and the disorganized microtubule pattern (488 nm, green). The scale bar is 20 μm for both images. (b) Time series of the organization on the lipid surface in presence of 88 kDa MC. The scale bar is 20 μm for all images. (c) Fluorescent recovery after photobleaching of the fluorescent lipid bilayer surface demonstrates it is a fluid. Fluorescence intensity recovers 70% after 180 s. The shaded region indicates standard deviation of multiple measurements ($n = 6$). Representative images are inset to demonstrate recovery. The scale bar is 10 μm.

for achieving fanlike patterns is a factor 100–1000 higher (Tables I and IV) than the bulk viscosity measurement from the experiments, because we expect that the surface has an additional viscous drag. Indeed, a recent paper from our laboratory measured the diffusion of single particles near the polymer brush surface and found a factor 200 reduction in the diffusion coefficient [42].

Overall, the simulations are able to recapitulate the fanlike patterns we observe experimentally on polymer brush surfaces, but the dynamics to achieve the pattern are not the same. For experiments, nucleating and growing bundles were highly mobile on the surface. As they grew, they rotated and settled into their final state. For simulations, high viscosities were needed to achieve fanlike patterns. The nucleating and growing microtubules and bundles were not mobile, and they only rotated upon meeting neighboring filaments. As discussed above, the experiments on lipid bilayer surfaces are not recapitulated well by simulations in the final state or in the dynamics. The lipid bilayer surface is able to disrupt the fanlike arrangement of microtubules, implying that the surface interactions have a significant impact on these beautiful patterns.

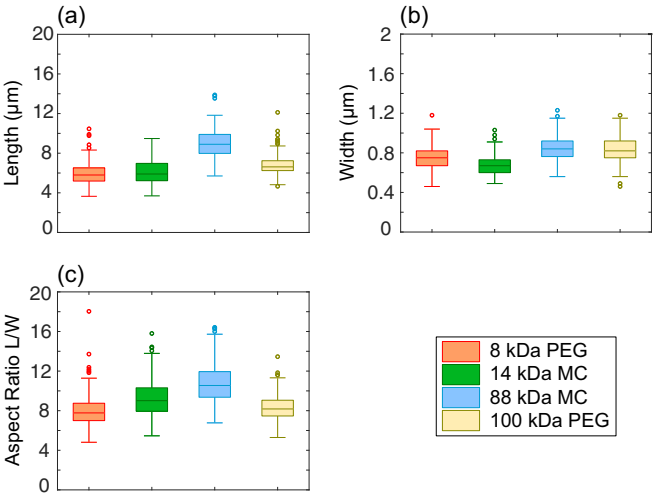

FIG. 8. Box-whisker plots of tactoid characteristics with 10% MAP65 on the polymer brush surface: (a) length of the tactoids, (b) width of the tactoids, and (c) aspect ratio of the tactoids. Tactoids are formed in presence of 8 kDa PEG (orange, $n = 205$), 14 kDa MC (green, $n = 217$), 88 kDa MC (blue, $n = 207$), 100 kDa PEG (yellow, $n = 240$).

B. Microtubule organization with MAP65

In our prior work, we were able to reproducibly form microtubule tactoids in the presence of MAP65 at a concentration of 10% bound [16]. Liquid crystal theory tells us that the competition between elastic deformation energy of the director or microtubule orientation field inside and anisotropic surface energy at the interface defines the shape of the tactoid and director field inside it. As we showed previously, the tactoids are homogeneous droplets with a constant director field along the major axis of the tactoid [16]. Boojums (virtual defects) are located at infinity, not at the poles, as for the bipolar case. We showed that microtubule tactoids are jammed or frozen inside the droplet, demonstrated by imperceptible microtubule turnover when probed using FRAP[16]. FRAP also showed that MAP65 turnover was fast due to the relatively weak binding constant, 1.2 μM [16].

1. Polymer surface with different crowders

Here, we are interested in examining the effect of different crowding agents on the formation, shape, and dynamics of these tactoids. For all experiments, 13.6 μM tubulin was used with 10% MAP65 to induce tactoid formation on polymer brush surfaces. In order to quantify the tactoid shape, we use a custom MATLAB code and manual measurements in FIJI, to measure the maximum length, $L = 2l$, where l is the half-maximum length, and width, $W = 2r$, where r is the half-maximum radius of imaged tactoids. We calculate the aspect ratio L/W (Table III). Tactoids that form on polymer surfaces in the presence of PEG or MC have subtle differences in their lengths [Fig. 8(a)]. The 88 kD MC made slightly longer tactoids than other crowders. Using the KS statistical tests, we find that the length measurements are all statistically different from one another (Appendix C, Table XIII). As we observed previously, the widths of the tactoids are in a small range from 500 to 1500 nm [Fig. 8(b)]. The 88 kD MC and 100 kD PEG

TABLE III. Tactoid features: mean length, mean width, mean aspect ratio, and dimensionless anchoring strength. The difference between the top four rows and the bottom four rows is that the data from the top rows were measured by hand using FIJI and the bottom rows were measured using MATLAB. As indicted, the first four columns are for polymer brush surfaces and last two columns are for lipid surfaces.

	Polymer brush surface				Lipid surface	
Crowders	8 kDa PEG (mean ± SD)	14 kDa MC (mean ± SD)	88 kDa MC (mean± SD)	100 kDa PEG (mean± SD)	88 kDa MC (mean ± SD)	100 kDa PEG (mean ± SD)
L (μm)	5.9 ± 1.0	6.1 ± 1.2	8.9 ± 1.4	6.8 ± 0.9	9.2 ± 1.1	7.7 ± 1.0
W (μm)	0.8 ± 0.1	0.7 ± 0.1	0.8 ± 0.1	0.8 ± 0.1	0.9 ± 0.1	0.9 ± 0.1
L/W	8 ± 1.7	9.2 ± 1.7	10.7 ± 1.9	8.3 ± 1.3	10.4 ± 1.7	8.9 ± 1.4
$\omega \sim$	16	21	28	17	27	20
L (μm)	5.6 ± 0.9	5.6 ± 1.1	8.8 ± 1.5	6.2 ± 0.9	8.8 ± 1.2	7.2 ± 1.0
W (μm)	0.9 ± 0.1	0.8 ± 0.1	1.0 ± 0.1	0.9 ± 0.1	1.0 ± 0.1	0.9 ± 0.1
L/W	6.3 ± 1.1	7.0 ± 1.5	9.0 ± 1.9	6.7 ± 1.0	9.3 ± 1.3	7.8 ± 1.4
$\omega \sim$	10	12	20	11	22	15

are statistically the same, and 8 kD PEG and 14 kD MC are statistically distinct from all other distributions (Appendix C, Table XIV). Since the diffraction limit of our microscope is about half the wavelength of the light we image, the widths are only about two to three times the diffraction limit, and are less reliable than the length measurements.

Using the lengths and widths, we calculate the aspect ratio for each crowder. We find that all the distributions are statistically distinct using the KS statistical test, and the data show a dependence on crowder type [Fig. 8(c), Appendix C, Table XV]. We observe that the aspect ratios of tactoids made in the presence of PEG are always smaller than those made with MC. Interestingly, the dependence of tactoid aspect ratios mirrored the trends we see for the fanlike patterns of self-organization in the absence of the MAP65 crosslinker [Tables II and III, Fig. 4(c-i) inset]. Given that we have directly measured that PEG changes the nucleation and growth of microtubules, this seems the most likely mechanism for the altered aspect ratios of these tactoids. In our prior work, we did not examine if the contour length of the microtubules altered the aspect ratio of the tactoids because we could not achieve the same experimental parameters for the highest concentrations of tubulin which gave shorter contour lengths. These current data imply that the nucleation and growth kinetics could impact the final aspect ratio of the tactoids.

2. *Lipid surface with different crowders*

On lipid surfaces, we are able to reproduce tactoids consistently in the presence of different crowders. We focus on the effects of the surface conditions for only 88 kDa MC and 100 kDa PEG. For these large polymers, we observe distinct differences in the lengths and aspect ratios comparing the 88 kDa MC and 100 kDa PEG, but not the widths (Fig. 9, Appendix C, Table XVI, Table XVII, and Table XVIII).

3. *Microtubule tactoid shapes cannot be explained by liquid crystal theory*

To compare our tactoid results to liquid crystal theory and attempt to elucidate the physical mechanisms controlling tactoid formation, we use the length, width, and aspect ratio measurements from all the data to examine the shape parameters (Fig. 10). We plot the aspect ratio L/W as a function of L, and find that the dependence appeared linear with a positive slope, $m = 1.21 \pm 0.01$ [Fig. 10(a), Appendix C, Table XIX]. The linear dependence indicates the constant width of the tactoids. The plot has a large scatter, which is due to the wide range of data for the lengths and widths [Fig. 10(a)]. Despite the scatter, this result suggests that the width is constant for all tactoids, regardless of the crowding agent and surface used [Fig. 10(a)]. Prior work on other systems of homogeneous tactoids have not observed any dependence of the aspect ratio on the length of the tactoids. For instance, homogeneous tactoids made from carbon nanotubes have been shown experimentally to display a constant aspect ratio as a function of tactoid length, implying that the length and width grew together [43]. The difference between prior systems and the microtubule system could be that our system is driven to condense using specific crosslinkers and is not fluidlike.

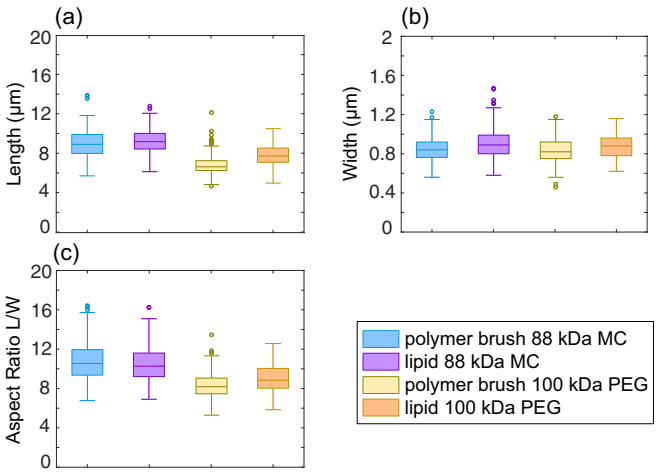

FIG. 9. Box-and-whisker plots of (a) length, (b) width, and (c) aspect ratio of tactoids in presence of two different crowders, 88 kDa MC and 100 kDa PEG, on polymer brush and lipid coated surfaces. For all plots, there are 88 kDa MC tactoids on the polymer brush surface (light blue, $n = 207$), 88 kDa MC tactoids on the lipid surface (purple, $n = 374$), 100 kDa PEG tactoids on the polymer brush surface (yellow, $n = 240$), and 100 kDa PEG tactoids on the lipid surface (orange, $n = 152$).

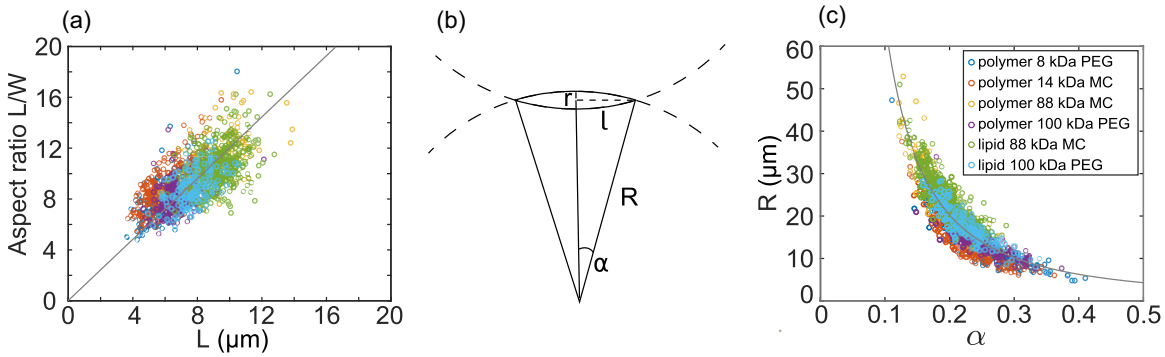

FIG. 10. Tactoid shape characteristics for all presented data. (a) Plot of tactoid aspect ratio vs tactoid length $L = 2l$ showing a slope equivalent to the constant width of the tactoids. (b) Diagram showing the relationship between quantitative parameters of the tactoid r, l, R, and α. (c) Plot of R vs α demonstrating a power law behavior due to the constant tactoid width. The gray lines in (a) and (c) represent fits to the data (Appendix C, Tables XIX and XX).

We can examine tactoid shape in another way, using two additional variables to characterize the tactoid: R and α. These parameters come from thinking of the tactoid surface as an arc of a circle with radius R making an angle 2α at the center [Fig. 10(b)]. These shape parameters can be related to the semimajor length $l = L/2$ and semiminor length $r = W/2$, as follows:

$$R = \frac{l^2 + r^2}{2r}, \tag{10}$$

$$\alpha = \sin^{-1}\left(\frac{2lr}{l^2 + r^2}\right). \tag{11}$$

We find that when we plot R as a function of α we see an inverse dependence. This dependence is another indicator that the width is constant in our system. When we fit the data for R vs α with a power law, it yields an exponent $\delta = -1.69 \pm 0.04$ [Fig. 10(c), Appendix C, Table XX]. This behavior is the opposite of what was seen previously in the case of actin tactoid condensates [6].

In the prior work, the actin tactoids were bipolar, so that the R dependence on α could be used to determine the rescaled Frank free energy constants for splay κ_1 and bending κ_3 [6]. Bipolar tactoids are described by the elastic energy terms as in Eq. (D2) (see Appendix D for details). Although our tactoids are not bipolar, if we were to use the same assumptions to fit our results, we would end up with a negative bending constant, which is nonphysical.

For homogeneous tactoids, which our microtubule tactoids appear to be, the surface energy term in free energy should dominate the energy landscape [Eq. (D3)]. Further, elastic terms are negligible because there are no distortions in the director field. In liquid crystal theory using scaling arguments and minimization of free energy via variational theory, it has been shown that ω, the ratio of the anchoring strength and the bare surface tension, is the sole parameter describing systems with homogeneous tactoids [4]. We calculated ω values using $L/W = 2\omega^{1/2}$ for $\omega \gg 1$. In our case, L/W is much larger than 1, as seen in Table III. Using the average value of L/W for our systems, we find that ω ranges from 16 to 28. These ω values are large compared to other systems [5,9,43].

Our tactoids are different from other system in a few ways. First, being a homogeneous tactoid, the aspect ratio does not stay constant with the length of the tactoid as would be predicted from liquid crystal theories and experiments. Second, the ω value is high although the tactoids are homogeneous. In our prior work, we demonstrated that microtubule tactoids are immobile and likely jammed within the tactoid [16]. Since the microtubules within the tactoids do not move, they do not behave like liquid droplets. Microtubule tactoid condensates might be more reminiscent of solid condensates in a liquid background—like the precipitation of crystals.

4. Tactoid growth dynamics

In order to help understand the mechanism of tactoid formation, we directly observe how a single tactoid nucleated and grew in time by quantifying the intensity profile as a function of time (Fig. 11(a)]. We plot only the intensity profile of the major axis over time as an example of the analysis [Fig. 11(b-i)]. When we plot the length of three tactoids as a function of time, we find that the tactoid growth displayed two distinct growth phases [Fig. 11(b-ii)]. In early times, the tactoid nucleates and grows quickly. The tactoid is short, likely having formed from subresolution, highly mobile microtubule filaments associating via the crosslinking protein. The tactoid length increases rapidly at a rate $v_t = 10.7 \pm 0.2$ nm/s (Appendix C, Table XXI), fit from $t = 0$ s until $t = 200$ s. This tactoid length growth rate suggests that this initial growth is because of microtubule elongation and not because of new microtubule addition, as this growth rate is one third of the microtubule growth rate in this tubulin concentration [38]. The time denoted $t = 0$ s is the time when the chamber is placed on the microscope, which was ≈1 min after the elongation mix is flowed through the chamber. At longer times, the tactoid length either reaches a stable state or shows very little growth with a slope 0.39 ± 0.02 nm/s (Appendix C, Table XXI).

Interestingly, the width of these initial assemblies is already in the range of 500–1500 nm, the same range we observe for all tactoids [Figs. 8(b) and 9(b)]. These data imply that the width of the tactoids is set very early in nucleation and growth, and changes little over time. We observe

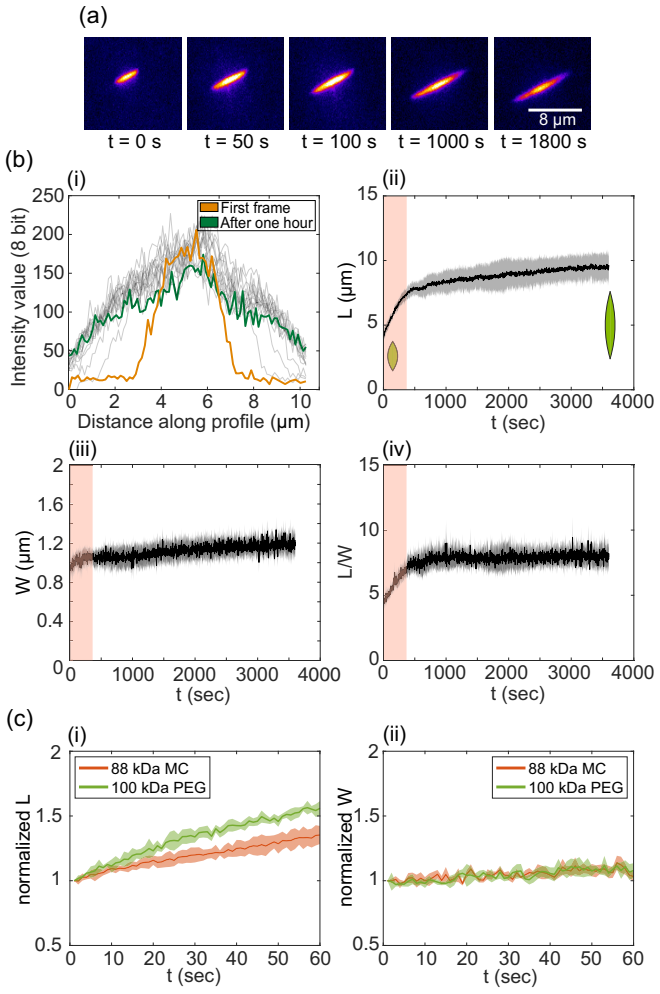

FIG. 11. (a) Time series of a single tactoid growth on the lipid surface in presence of 100 kDa PEG as the crowder. Here $t = 0$ s represents the starting point of data acquisition. (b) Tactoid growth characterization. (b-i) Intensity distribution along tactoid length for the first frame (orange line), over time (gray lines) and after 1 h (green line). (b-ii) Tactoid length L plotted over time. (b-iii) Tactoid width W plotted over time. (b-iv) Tactoid aspect ratio, L/W plotted over time. For (b-ii)–(b-iv), three tactoids from the same video are averaged. Data are taken in the presence of 88 kDa MC on the lipid surface. (c) Tactoid growth rate comparison in presence of two crowders 88 kDa MC (red shaded curve, $n = 4$) and 100 kDa PEG (green shaded curve, $n = 3$) on the lipid surface within the first minute: (c-i) normalized tactoid length L and (c-ii) normalized tactoid width W. The shaded regions indicate the standard deviation of the mean.

a small change in width over time, with a slope of 0.048 ± 0.002 nm/s [Fig. 11(b-iii), Appendix C, Table XXI].

The aspect ratio L/W also has two phases as a function of time [Fig. 11(b-iv)]. Since the width does not change much, even in the initial fast-growing phase, the aspect ratio's trend follows that of the length, with an initial fast growing rate of $r_t = 0.0088 \pm 0.0006$ s^{-1} (Appendix C, Table XXI). At the later phase, the aspect ratio does not change and has a constant aspect ratio of $L/W = 7.7 \pm 0.1$ (Appendix C, Table XXI), which we find by fitting the data from $t = 2000$ to 3600 s to a line and determining the offset.

We also observe a change in tactoid length growth rate in initial times in presence of different crowders. In presence of 100 kDa PEG we observe faster tactoid length growth than tactoids in presence of 88 kDa PEG. We have normalized the tactoid length to observe this difference as shown in Fig. 11(c-i). Initial tactoid length growth is likely due to microtubule elongation. Once again, our observation bolsters the conclusion that the crowders affect the growth rate. The trend is similar to Fig. 6(c), which suggests crowders affect the growth timescale, and that is reflected in length difference. The crowders do not cause variation in the tactoid width [Fig. 11(c-ii)].

Overall, when examining the tactoids and comparing to prior liquid crystal theory and experiment, we find that the microtubule tactoids are unique. They have solidlike properties with little rearrangement inside themselves. The microtubule tactoid system did not display the homogeneous to bipolar transition. In other entropically driven systems it has been predicted and shown that this transition happens when the size or the volume of the tactoid crosses a threshold value, which depends on κ from elastic terms and ω from surface terms. The homogeneous to bipolar transition was observed experimentally in the CNT system [44] and amyloid fibril systems [9].

The primary physical aspect of microtubule tactoids that makes them inaccessible to liquid crystal theory is that the tactoid width is approximately constant in all conditions. Due to the limited width, the aspect ratio depends entirely on tactoid length. Further, the width was unaffected by experimental parameters such as the crowding agent or the surface of the chamber.

There are several possible reasons why the width is constant. First, there is a crosslinker causing condensation of the tactoids instead of being entropically driven, like previous systems [6,9,44]. There was a prior report of actin filament tactoid formation driven by an actin-associated protein crosslinker that was bipolar, behaved as a liquid with a fluid interior, and was capable of coalescence [5,45]. The differences between the microtubule and actin tactoids condensed with crosslinkers could be caused by the crosslinker affinity, flexibility, or filament length control, which were different for each of these systems. Future studies using engineered MAP65 crosslinkers with altered physical characteristics or binding affinities could begin to probe these possibilities.

Another mechanism could be due to the presumably altered affinity of the crosslinker when bound. The equilibrium dissociation constant for MAP65 to bind to single microtubules is $K_D \sim 1.2$ μM, indicating weak affinity and a fast turnover rate [22]. Despite the relatively weak binding, MAP65 can immobilize the microtubules within the tactoid [16] and even slow microtubule gliding driven by strong kinesin-1 motors [18]. Other works have also demonstrated that MAP65 and its analogs have a higher affinity for microtubules that are crosslinked in an antiparallel manner compared to its affinity on a single filament which can cause compaction forces to shorten the overlapping bundled regions between microtubules [18,19,46,47]. If there is strong binding within the bundle, that could control the director field inside the tactoid and result in $\kappa > \omega$. For future models, adding a specific "crosslinking" term in the free energy expression could be used to describe this system more accurately.

An additional consequence of altered affinity of MAP65 when bound is that the concentration outside of the tactoids would become depleted compared to the concentration inside where the MAP65 should be sequestered. If a new microtubule or tactoid tries to bind to the already bundled filaments, there could be insufficient available MAP65 to allow binding or coalescence. Further, already nucleated and polymerized microtubules are slower to diffuse and would not be able to join tactoids easily compared to free dimers. Such new microtubules are unlikely to be nucleated once significant growth has started, due to the depletion of dimers from the environment, so it is more likely for the length to continue to grow than the width. Thus, the width limit could be a natural consequence of the nucleation and growth kinetics of microtubules.

Finally, the fixed width could be explained by other physical phenomena. Limited width in assemblies has been explored theoretically by kinetically arrested aggregation models [48], self-assembly models with long-range interaction schemes [49], as well as chirality and geometrical packing frustration problems [50]. Microtubules have an intrinsic chirality present in their lattice, most clearly shown at the lattice "seam." If MAP65 binding templates off the microtubule lattice, the tactoids should be chiral bundles as well. This inherent chirality could result in packing frustration which limits the width in the assembly [50,51].

In support of the idea of a chiral tactoid, prior work on the structure of mitotic spindles has shown that the overlapping microtubules, which are coated with MAP65-like proteins, display a helical twist of the filaments of the spindle [52]. Cross-sectional studies of microtubule bundles in the presence of crowders have shown that increasing depletion can alter the packing from square to hexagonal packing [53,54], but they did not examine if there was chirality. Similar high resolution studies using cryoelectron microscopy on microtubule tactoids have yet to be performed, but they may show a chirality and square packing to accommodate the antiparallel preference between filaments.

IV. CONCLUSIONS

Using bottom-up reconstitution experiments, we examine how entropic forces can control pattern formation in a microtubule system with and without crosslinkers. We find that the quantitative metrics of the organization subtly depend on the crowder. We are able to perform simulations in the absence of crosslinkers that show the quantitative metrics of the pattern are most likely controlled by the contour length. The contour length of microtubules in our system is a direct consequence of the nucleation and growth kinetics. We test if the crowding agents alter the nucleation and growth kinetics, and we find the same trends in growth rates as observed in the pattern metrics. These results imply that the crowding effects are likely only changing due to altered contour lengths from altered growth kinetics. We also test the pattern formation in the presence of the crosslinkers to create tactoids and find the same effects due to different crowding agents, again implying that the nucleation and growth kinetics affect the tactoids metrics.

We test if the surface treatment affected the pattern with and without crosslinkers. We find that the surface pattern without crosslinkers is less reproducible on lipid bilayer surfaces despite the increased fluidity of the surface. Tactoid shape metrics are unaffected by the presence of the lipid bilayer.

Using our quantitative metrics, we test our tactoids against existing liquid crystal theories. The tactoids are not comparable to liquid crystal theory because the condensed microtubule phase is not liquid, but appears solid. In addition, the width of the condensed homogeneous tactoids is constant regardless of crowders.

In this paper, the only dynamic component is microtubule growth, which is halted when the free tubulin is exhausted. The mitotic spindle and other biological condensed tactoid systems are fluid and display steady-state dynamics. In order to capture these exciting activities, we propose future experiments should include active components, such as motor proteins. Indeed, such experiments have resulted in active nematics of microtubule bundles, asters, and vortices [34,35,55–58]. Other possible directions to explore to increase the fluidity of these condensates include adding enzymes, such as depolymerizing kinesins or microtubule severing enzymes, to limit microtubule length. Moreover, addition of nucleating centers to restrict nucleation and growth, or crosslinker affinity alteration, or addition of different ionic species are future directions to explore.

ACKNOWLEDGMENTS

This work was funded by NSF Grant No. BIO-1817926 and partially funded from the Keck Foundation to Dr. R. Robertson-Anderson, M. Das, M. Rust, and J.L.R.

Experiments were performed by S.S., L.H., and R.Q. Initial analysis was performed by L.H. and R.Q. S.S. and J.L.R. composed the original paper. S.S., L.H., R.Q., and J.L.R. edited the paper.

APPENDIX A: CROWDER CHARACTERIZATION

In our experiments, two types of crowders (methylcellulose and polyethylene glycol) are added to the system, with different molecular weights, and % (w/v) concentrations to modulate the depletion forces. In our experiments, we only use dilute polymer solutions where polymers are hydrodynamically separated and cannot interact with each other. Once the concentration of polymer, c, crosses the critical overlap concentration c^*, polymers become entangled and overlapped. In the dilute regime $c < c^*$, these blob configurations are characterized by the radius of gyration R_g. A scaling relation, $R_g = K_R M_W^{\nu}$, connects R_g with weight-average molecular weight M_W, where ν is the Flory exponent, and K_R is an empirical constant of proportionality. Similarly, the intrinsic viscosity $[\eta] = \lim_{c\to 0} \frac{\eta-\eta_0}{c\eta_0}$ is related to M_W by the Mark-Howink-Sakurada (MHS) equation, $[\eta] = K_\eta M_W^{\alpha}$, where c is the solute concentration, α is the MHS exponent, K_η is the empirical constant of proportionality, and η and η_0 are the solution and solvent viscosity, respectively. The polynomial expression of osmotic pressure Π is obtained via virial expansion in terms of molar concentration C [59]:

$$\Pi = RT[C + aC^2 + bC^3 + \ldots] \tag{A1}$$

where R is the universal gas constant and T is temperature in K, and a and b are virial coefficients. For low polymer concentration like our experiment, the lower bound can be

TABLE IV. Crowder characteristics.

Crowders	8 kDa PEG	14 kDa MC	88 kDa MC	100 kDa PEG
K_R (nm)	0.021[c]	0.054[a]	0.054[a]	0.021[c]
ν	0.583[c]	0.576[a]	0.576[a]	0.583[c]
K_η (ml/g)	0.0488[b]	0.102[a]	0.102[a]	0.0064[b]
α	0.66[b]	0.704[a]	0.704[a]	0.82[b]
R_g (nm) $\sim$	4[c]	13[a]	38[a]	17[c]
η_{ref} (cP)	0.91	0.85	1.13	0.93
η_{exp} (cP)	0.97	0.96	2.13	0.98
c^*% (w/v)	4.7	1.21	0.33	0.72
c% (w/v)	1	0.12	0.15	0.25
c in μM	1250	85	17	25
$\Pi\,(\frac{N}{m^2})$ $>$	3221	219	43	64

[a]Reference [60].
[b]Reference [61].
[c]References [62,63].

well estimated by setting $\Pi \sim CRT$ ignoring higher order terms.

For each polymer, physical properties such as viscosity η, radius of gyration R_g, and critical entanglement concentration c^* are estimated and shown in Table IV. PEGs are highly soluble, linear, inert polymers, whereas MCs are negatively charged, branched, polymers that strongly influence the macroscopic viscosity. For MCs, our parameters are estimated from [60]. The R_g and M_W are insensitive to temperature within the range 15–60 °C whereas η depends on temperature, and experiments were performed at 15 °C and MC concentrations of 0.03% (w/v) (dilute regime) in the referenced article [60]. For aqueous PEG solution at 35 °C, the viscosity parameters are estimated from data in [61]. The R_g value and $c^* = \frac{M_W}{\frac{4}{3}\pi R_g^3 N_A}$, where N_A is Avogadro's number, are extrapolated for our M_W from [62,63]. We estimate the viscosity, η_{ref} from the given values of K_η and α in [60–63]. In addition, since our experiments are performed at 37 °C to enhance microtubule growth, we also measure the viscosity independently of η_{exp} in Table IV.

APPENDIX B: CYTOSIM DEPLETION VS NO DEPLETION COMPARISON

In our CYTOSIM simulation, we implemented an effective depletion force using an attractive spring force, Eq. (8). Although this has been used in the literature previously [35,36], a more appropriate model for depletion force is a Derjaguin-like approximation. When we repeat our simulations in the absence of the attractive spring force, we find the trend is unaffected. We compare the results from simulations without and with attractive spring force for specific packing fractions to compare over different contour lengths. In Fig. 12 we showed that without attractive depletion force the model still follows the same trend of dependence on the contour length. This is the main takeaway, and it is independent of whether we use the attractive force or not. Quantitatively, we find that the average domain size $\overline{\langle s \rangle}$ and mean correlation length $\overline{\xi}$ are slightly higher without the attractive force.

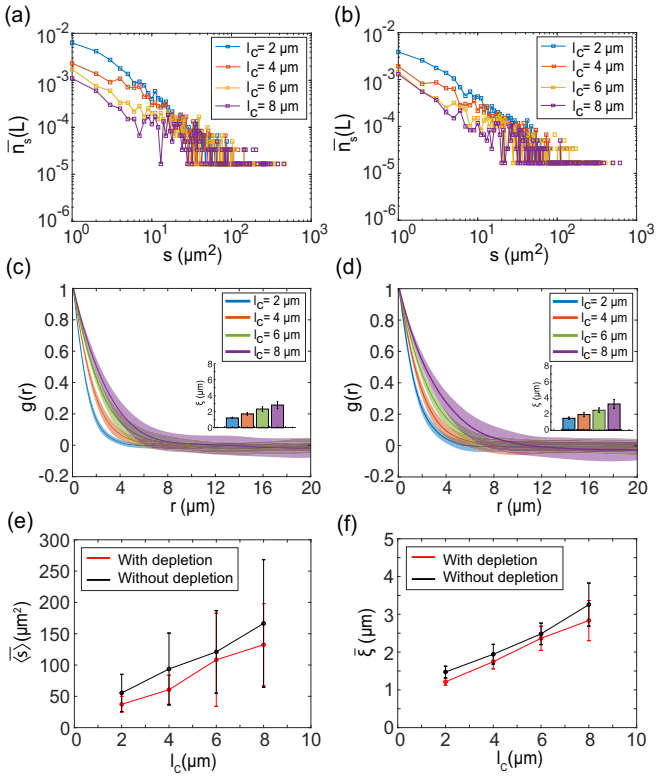

FIG. 12. (a), (c) Data from the CYTOSIM model with attractive force comparing (a) domain size distribution and (c) the radially averaged mean autocorrelation function for different contour lengths. (b, d) Data from the CYTOSIM model without attractive force comparing (b) domain size distribution and (d) the radially averaged mean autocorrelation function comparing different contour lengths. All data shown for $\phi = 0.75$ ($n = 6$), l_c are 2 μm (blue squares), 4 μm (red squares), 6 μm (yellow squares), and 8 μm (purple squares). Comparison of (e) the average domain size $\overline{\langle s \rangle}$ and (f) the mean correlation length $\overline{\xi}$ for no attractive force (black) and with attractive force (red).

APPENDIX C: STATISTICAL ANALYSIS AND FIT DATA

This Appendix shows parameters from Kolmogorov-Smirnov statistical test (KS test) and fit equation parameters to draw quantitative inference to our results. The KS test is a nonparametric test applied to empirical data to test whether the difference in two samples is statistically significant; in other terms, it tests the hypothesis where two samples came from the same distribution or not. We report the p-values after comparing two samples using MATLAB function kstest2.

TABLE V. P values from two sample KS tests performed on domain area data for different crowders as described in results and discussion [Fig. 4(b-i)].

	8 kDa	14 kDa	88 kDa	100 kDa
8 kDa PEG		3.3×10^{-6}	2.7×10^{-5}	8.1×10^{-5}
14 kDa MC			0.1428	0.6937
88 kDa MC				0.0749
100 kDa PEG				

TABLE VI. P values from two sample KS tests performed on domain area data for different tubulin concentrations as described in results and discussion [Fig. 4(b-ii)].

l	1.1 μm	2.5 μm	6.25 μm
1.1 μm		4.0×10^{-6}	8.2×10^{-14}
2.5 μm			4.9×10^{-6}
6.25 μm			

TABLE VII. P values from two sample KS tests performed on domain area data for CYTOSIM simulation as described in results and discussion [Fig. 4(b-iii)].

l	2 μm	4 μm	6 μm	8 μm
2 μm		2.6×10^{-18}	1.4×10^{-19}	1.6×10^{-20}
4 μm			0.011	5.6×10^{-6}
6 μm				0.0965
8 μm				

TABLE VIII. P values from two sample KS tests performed on correlation length for different crowders as described in results and discussion [Fig. 4(c-i) inset].

	8 kDa	14 kDa	88 kDa	100 kDa
8 kDa PEG		0.2464	0.0060	0.0760
14 kDa MC			0.0067	0.0167
88 kDa MC				1.7×10^{-6}
100 kDa PEG				

TABLE IX. P values from two sample KS tests performed on correlation length for different tubulin concentration as described in results and discussion [Fig. 4(c-ii) inset].

l	1.1 μm	2.5 μm	6.25 μm
1.1 μm		1.4×10^{-4}	8.6×10^{-11}
2.5 μm			2.5×10^{-19}
6.25 μm			

TABLE X. P values from two sample KS tests performed on correlation length for CYTOSIM data as described in results and discussion [Fig. 4(c-iii) inset].

l	2 μm	4 μm	6 μm	8 μm
2 μm		7.4×10^{-11}	8.8×10^{-12}	8.8×10^{-12}
4 μm			4.0×10^{-9}	7.4×10^{-11}
6 μm				0.0029
8 μm				

TABLE XI. Fit parameters for the number scaling and the area scaling in log-log scale using the equation $y = ax + b$ [Figs. 5(a) and 5(c)].

	a[a]	b[a]	R squared
Number scaling	-1.6 ± 0.1	-3.1 ± 0.1	0.9803
Area scaling	1.5 ± 0.1	3.4 ± 0.1	0.9831

[a]All data presented are value ± 95% confidence bound.

TABLE XII. Normalized absorbance data fit parameters from turbidity measurement, using Eq. (1) [Fig. 6(b)].

	a[a]	b[a]	t_0 (s)[a]	τ (s)[a]	R squared
Tubulin	0.994	1.05	1266	284.7	0.9952
	±0.007	±0.03	±24	±22.2	
8 kDa	0.991	1.10	751.4	193.9	0.9949
	±0.009	±0.04	±20.4	±16.1	
14 kDa	0.989	1.01	1664	228.1	0.9986
	±0.008	±0.01	±10	±9.8	
88 kDa	0.984	1.01	1377	252.8	0.9985
	±0.008	±0.01	±12	±10.9	
100 kDa	0.984	1.01	1093	184.1	0.9973
	±0.008	±0.02	±13	±11.3	

[a]All data presented are value ± 95% confidence bound.

TABLE XIII. P values from two sample KS tests performed on tactoid length for different crowders on the polymer brush surface as described in results and discussion [Fig. 8(a)].

	8 kDa	14 kDa	88 kDa	100 kDa
8 kDa PEG		0.04	5.2×10^{-60}	1.1×10^{-20}
14 kDa MC			5.2×10^{-49}	1.1×10^{-16}
88 kDa MC				4.6×10^{-46}
100 kDa PEG				

TABLE XIV. P values from two sample KS tests performed on tactoid width for different crowders on the polymer brush surface as described in results and discussion [Fig. 8(b)].

	8 kDa	14 kDa	88 kDa	100 kDa
8 kDa PEG		5.0×10^{-11}	9.5×10^{-11}	1.9×10^{-8}
14 kDa MC			4.1×10^{-37}	1.5×10^{-34}
88 kDa MC				0.8034
100 kDa PEG				

TABLE XV. P values from two sample KS tests performed on tactoid aspect ratio for different crowders on the polymer brush surface as described in results and discussion [Fig. 8(c)].

	8 kDa	14 kDa	88 kDa	100 kDa
8 kDa PEG		1.1×10^{-12}	7.9×10^{-36}	0.0055
14 kDa MC			2.3×10^{-13}	8.9×10^{-7}
88 kDa MC				8.8×10^{-36}
100 kDa PEG				

TABLE XVI. P values from two sample KS tests performed on tactoid length for different crowders on the lipid surface as described in results and discussion [Fig. 9(a)].

	100 kDa PEG
88 kDa MC	7.4×10^{-27}

TABLE XVII. P values from two sample KS tests performed on tactoid width for different crowders on the lipid brush surface as described in results and discussion [Fig. 9(b)].

	100 kDa PEG
88 kDa MC	0.6167

TABLE XVIII. P values from two sample KS tests performed on tactoid aspect ratio for different crowders on the lipid surface as described in results and discussion [Fig. 9(c)].

	100 kDa PEG
88 kDa MC	2.5×10^{-13}

TABLE XIX. Length vs aspect ratio fit parameters for all tactoids, using the equation $y = mx$ [Fig. 10(a)].

	m $(1/\mu\text{m})$[a]	R squared
Initial	1.21 ± 0.01	0.2573

[a]All data presented are value ± 95% confidence bound.

TABLE XX. α vs R fit parameters for all tactoids, using the equation $y = Ax^{\delta}$ [Fig. 10(c)].

	A[a]	δ[a]	R squared
Later	1.3 ± 0.1	-1.69 ± 0.04	0.8113

[a]All data presented are value ± 95% confidence bound.

TABLE XXI. Tactoid growth characteristics fit parameters, using the equation $y = ax + b$ (Fig. 11).

Parameter	a[a]	b[a]	R squared
Length (μm) (0 to 200 s)	$(10.7 \pm 0.2) \times 10^{-3}$	4.24 ± 0.03	0.9892
Length (μm) (2000 to 3600 s)	$(0.39 \pm 0.02) \times 10^{-3}$	8.16 ± 0.04	0.7689
Width (μm) (200 to 3600 s)	$(0.048 \pm 0.002) \times 10^{-3}$	1.029 ± 0.004	0.6406
Aspect ratio (0 to 200 s)	$(8.8 \pm 0.6) \times 10^{-3}$	4.41 ± 0.07	0.89
Aspect ratio (2000 to 3600 s)	$(0.11 \pm 0.04) \times 10^{-3}$	7.7 ± 0.1	0.0310

[a]All data presented are value ± 95% confidence bound.

APPENDIX D: TACTOID SCALES

In this Appendix we discuss briefly the theoretical aspect of the tactoid assembly previously described [3,4,64,65]. The total free energy functional of a nematic tactoid can be written in general form as

$$F = F_E + F_S \tag{D1}$$

where F_E is the bulk elastic energy and accounts for director field deformation inside the tactoid, and F_S is the interfacial energy term. The elastic term in the Frank energy, which is integrated over volume V, can be written down as

$$F_E = \int_V d^3\mathbf{r}\Big[\frac{K_1}{2}(\nabla\cdot\mathbf{n})^2 + \frac{K_2}{2}(\mathbf{n}\cdot\nabla\times\mathbf{n})^2 + \frac{K_3}{2}(\mathbf{n}\times\nabla\times\mathbf{n})^2 - K_{24}\nabla\cdot[\mathbf{n}\nabla\cdot\mathbf{n} + \mathbf{n}\times(\nabla\times\mathbf{n})]\Big]$$

in terms of director field $\mathbf{n}(\mathbf{r})$. Here, K_1, K_2, K_3, and K_{24} are splay, twist, bend, and saddle-splay deformation modes, respectively. Usually, the twist term K_2 is dropped assuming a no-twist condition. The K_{24} term can be absorbed into K_1 to give

$$F_E = \int_V d^3\mathbf{r}\Big[\frac{K_1}{2}(\nabla\cdot\mathbf{n})^2 + \frac{K_3}{2}(\mathbf{n}\cdot\nabla\times\mathbf{n})^2\Big]. \tag{D2}$$

The interfacial surface energy term, which is integrated over the tactoid surface, has two components with accompanying parameters. The first component comes from the isotropic surface energy, which is driven by the interfacial tension, τ. The second term introduces anisotropy in the surface energy term, which is driven by the ratio of the anchoring strength and interfacial tension, ω, a measure of how directors interact with the interface:

$$F_S = \tau\int_S d^2\mathbf{r}\{1 + \omega(\mathbf{q}\cdot\mathbf{n})^2\}. \tag{D3}$$

Here $\mathbf{q}$ is the unit normal to the interfacial surface. As described, this system can be parametrized using R and α. From a simple scaling argument, it can be shown that the bulk elastic deformation cost should scale as $\approx KR^3$ multiplied by $\frac{1}{R^2}$, which accounts for square derivatives, i.e., $\approx KR$ and surface anchoring energy will have $\approx \omega R^2$ scaling. The total free energy, written in terms of these two independent variables, takes the form

$$\begin{aligned} F &= F_E + F_S \\ &= \sum_{i=1,3} K_i R f_E^{(i)}(\alpha) + \tau R^2[f_S(\alpha) + \omega f_W(\alpha)] \end{aligned}$$

$$\Rightarrow \widetilde{F} = \sum_{i=1,3}\kappa_i\psi_E^{(i)}(\alpha) + \psi_S(\alpha) + \omega\psi_W(\alpha) \tag{D4}$$

where $\widetilde{F} = \frac{F}{\tau V^{\frac{2}{3}}}$, $\kappa_i = \frac{K_i}{\tau V^{\frac{1}{3}}}$, $\psi_E^{(i)}(\alpha) = \frac{f_E^{(i)}(\alpha)}{v(\alpha)^{\frac{1}{3}}}$, and $\psi_{W,S}(\alpha) = \frac{f_{W,S}(\alpha)}{v(\alpha)^{\frac{2}{3}}}$ are the scaled variables. The surface area and volume

are defined as $A = R^2 f_S(\alpha)$ and $V = R^3 v(\alpha)$:

$$f_S(\alpha) = 4\pi(\sin\alpha - \alpha\cos\alpha),$$
$$v(\alpha) = 2\pi\left(\sin\alpha - \alpha\cos\alpha - \frac{\sin^3\alpha}{3}\right).$$

The director field inside a tactoid is related to its size or volume. There is a crossover from the homogeneous to the bipolar director field as volume gets larger, predicted from theory [4] and verified in the experiments with carbon nanotubes in chlorosulfonic acid [44]. The homogeneous director field configuration is elastically rigid and has an unperturbed director, $\mathbf{n}(\mathbf{r}) = \mathbf{n}$. In the small volume limit, $V \to 0$, $1 \ll \omega < \kappa$, therefore the elastic deformation term $\psi_E^{(i)}(\alpha)$ must be zero as it introduces a huge contribution from a small perturbation in the director field. Only surface terms remain with ω being the only scaled parameter in the problem. This condition defines the crossover volume, $V \sim (\frac{K}{\tau\omega})^3$. From the Wulff construction, it has been predicted that aspect ratio $l/r = 2\omega^{1/2}$ for $\omega \gg 1$.

[1] D. Oriola, D. J. Needleman, and J. Brugués, The physics of the metaphase spindle, Annual Review of Biophysics **47**, 655 (2018).

[2] J. Brugués and D. Needleman, Physical basis of spindle self-organization, Proc. Natl. Acad. Sci. USA **111**, 18496 (2014).

[3] A. V. Kaznacheev, M. M. Bogdanov, and S. A. Taraskin, The nature of prolate shape of tactoids in lyotropic inorganic liquid crystals, J. Exp. Theor. Phys. **95**, 57 (2002).

[4] P. Prinsen and P. van der Schoot, Shape and director-field transformation of tactoids, Phys. Rev. E **68**, 021701 (2003).

[5] K. L. Weirich, S. Banerjee, K. Dasbiswas, T. A. Witten, S. Vaikuntanathan, and M. L. Gardel, Liquid behavior of cross-linked actin bundles, Proc. Natl. Acad. Sci. USA **114**, 2131 (2017).

[6] P. W. Oakes, J. Viamontes, and J. X. Tang, Growth of tactoidal droplets during the first-order isotropic to nematic phase transition of F-actin, Phys. Rev. E **75**, 061902 (2007).

[7] D. R. Scheff, K. L. Weirich, K. Dasbiswas, A. Patel, S. Vaikuntanathan, and M. L. Gardel, Tuning shape and internal structure of protein droplets via biopolymer filaments, Soft Matter **16**, 5659 (2020).

[8] G. Nyström, M. Arcari, and R. Mezzenga, Confinement-induced liquid crystalline transitions in amyloid fibril cholesteric tactoids, Nat. Nanotechnol. **13**, 330 (2018).

[9] M. Bagnani, G. Nyström, C. De Michele, and R. Mezzenga, Amyloid fibrils length controls shape and structure of nematic and cholesteric tactoids, ACS Nano **13**, 591 (2019).

[10] J. D. Bernal and I. Fankuchen, X-ray and crystallographic studies of plant virus preparations. I. Introduction and preparation of specimens. II. Modes of aggregation of the virus particles, J. Gen. Physiol. **25**, 111 (1941).

[11] H. Maeda, An atomic force microscopy study for the assembly structures of tobacco mosaic virus and their size evaluation, Langmuir **13**, 4150 (1997).

[12] Z. Dogic and S. Fraden, Development of model colloidal liquid crystals and the kinetics of the isotropic-smectic transition, Phil. Trans. R. Soc. A **359**, 997 (2001).

[13] Z. Dogic, Surface Freezing and a Two-Step Pathway of the Isotropic-Smectic Phase Transition in Colloidal Rods, Phys. Rev. Lett. **91**, 165701 (2003).

[14] L. Tortora, H. S. Park, S. W. Kang, V. Savaryn, S. H. Hong, K. Kaznatcheev, D. Finotello, S. Sprunt, S. Kumar, and O. D. Lavrentovich, Self-assembly, condensation, and order in aqueous lyotropic chromonic liquid crystals crowded with additives, Soft Matter **6**, 4157 (2010).

[15] L. Onsager, The effects of shape on the interaction of colloidal particles, Ann. NY Acad. Sci. **51**, 627 (1949).

[16] B. Edozie, S. Sahu, M. Pitta, A. Englert, C. F. Do Rosario, and J. L. Ross, Self-organization of spindle-like microtubule structures, Soft Matter **15**, 4797 (2019).

[17] C. Zhu, E. Lau, R. Schwarzenbacher, E. Bossy-Wetzel, and W. Jiang, Spatiotemporal control of spindle midzone formation by PRC1 in human cells, Proc. Natl. Acad. Sci. USA **103**, 6196 (2006).

[18] J. Pringle, A. Muthukumar, A. Tan, L. Crankshaw, L. Conway, and J. L. Ross, Microtubule organization by kinesin motors and microtubule crosslinking protein MAP65, J. Phys.: Condens. Matter **25**, 374103 (2013).

[19] R. Subramanian, E. M. Wilson-Kubalek, C. P. Arthur, M. J. Bick, E. A. Campbell, S. A. Darst, R. A. Milligan, and T. M. Kapoor, Insights into antiparallel microtubule crosslinking by PRC1, a conserved nonmotor microtubule binding protein, Cell **142**, 433 (2010).

[20] H. Li, T. Mao, Z. Zhang, and M. Yuan, The AtMAP65-1 cross-bridge between microtubules is formed by one dimer, Plant Cell Physiol. **48**, 866 (2007).

[21] J. Chan, C. G. Jensen, L. C. W. Jensen, M. Bush, and C. W. Lloyd, The 65-kDa carrot microtubule-associated protein forms regularly arranged filamentous cross-bridges between microtubules, Proc. Natl. Acad. Sci. USA **96**, 14931 (1999).

[22] A. Tulin, S. McClerklin, Y. Huang, and R. Dixit, Single-molecule analysis of the microtubule cross-linking protein MAP65-1 reveals a molecular mechanism for contact-angle-dependent microtubule bundling, Biophys. J. **102**, 802 (2012).

[23] H. Li, M. Yuan, and T. Mao, AtMAP65-1 binds to tubulin dimers to promote tubulin assembly, J. Biochem. Mol. Biol. **40**, 218 (2007).

[24] T. Mao, L. Jin, H. Li, B. Liu, and M. Yuan, Two microtubule-associated proteins of the Arabidopsis MAP65 family function differently on microtubules, Plant Physiol. **138**, 654 (2005).

[25] K. T. Stanhope and J. L. Ross, Microtubules, MAPs, and Motor Patterns, *Methods in Cell Biology*, Vol. 128 (Elsevier, Amsterdam, 2015), Chap. 2, pp. 23–28.

[26] R. Dixit and J. L. Ross, Studying plus-end tracking at single molecule resolution using TIRF microscopy, in *Methods in Cell Biology, Microtubules*, In Vitro Vol. 95, edited by Leslie Wilson and J. J. Correia (Academic, New York, 2010), Chap. 27, pp. 543–554.

[27] P. H. Schummel, M. Gao, and R. Winter, Modulation of the polymerization kinetics of α/β-tubulin by osmolytes and macromolecular crowding, Chem. Phys. Chem. **18**, 189 (2017).

[28] D. Stauffer and A. Aharony, *Introduction to Percolation Theory* (Taylor & Francis, London, 1992).

[29] C. Robertson, Theory and practical recommendations for autocorrelation-based image correlation spectroscopy, J. Biomed. Opt. **17**, 080801 (2012).
[30] S. L. Veatch, B. B. Machta, S. A. Shelby, E. N. Chiang, D. A. Holowka, and B. A. Baird, Correlation functions quantify super-resolution images and estimate apparent clustering due to over-counting, PLoS ONE **7**, e31457 (2012).
[31] N. Otsu, A threshold selection method from gray-level histograms, IEEE Trans. Syst. Man Cybern. Part A Syst. **9**, 62 (1979).
[32] F. Nedelec and D. Foethke, Collective Langevin dynamics of flexible cytoskeletal fibers, New J. Phys. **9**, 427 (2007).
[33] J. Rickman, F. Nédélec, and T. Surrey, Effects of spatial dimensionality and steric interactions on microtubule-motor self-organization, Phys. Biol. **16**, 046004 (2019).
[34] J. Roostalu, J. Rickman, C. Thomas, F. Nédélec, and T. Surrey, Determinants of polar versus nematic organization in networks of dynamic microtubules and mitotic motors, Cell **175**, 796 (2018).
[35] T. Strübing, A. Khosravanizadeh, A. Vilfan, E. Bodenschatz, R. Golestanian, and I. Guido, Wrinkling instability in 3D active nematics, Nano Lett. **20**, 6281 (2020).
[36] G. Letort, A. Z. Politi, H. Ennomani, Manuel Théry, F. Nedelec, and L. Blanchoin, Geometrical and mechanical properties control actin filament organization, PLoS Comput. Biol. **11**, e1004245 (2015).
[37] A. A. Hyman, S. Salser, D. N. Drechsel, N. Unwin, and T. J. Mitchison, Role of GTP hydrolysis in microtubule dynamics: Information from a slowly hydrolyzable analogue, GMPCPP, Mol. Biol. Cell **3**, 1155 (1992).
[38] J. Rickman, C. Duellberg, N. I. Cade, L. D. Griffin, and T. Surrey, Steady-state eb cap size fluctuations are determined by stochastic microtubule growth and maturation, Proc. Natl. Acad. Sci. USA **114**, 3427 (2017).
[39] W. Herzog and K. Weber, Microtubule formation by pure brain tubulin in vitro. the influence of dextran and poly(ethylene glycol), Eur. J. Biochem. **91**, 249 (1978).
[40] J. C. Lee and L. L. Y. Lee, Interaction of Calf Brain Tubulin with Poly(ethylene glycols), Biochemistry **18**, 5518 (1979).
[41] S. Musall, MATLAB central file exchange-stdshade, 2020.
[42] M. Xu, J. L. Ross, L. Valdez, and A. Sen, Direct Single Molecule Imaging of Enhanced Enzyme Diffusion, Phys. Rev. Lett. **123**, 128101 (2019).
[43] N. Puech, E. Grelet, P. Poulin, C. Blanc, and P. van der Schoot, Nematic droplets in aqueous dispersions of carbon nanotubes, Phys. Rev. E **82**, 020702 (2010).
[44] V. Jamali, N. Behabtu, B. Senyuk, J. A. Lee, I. I. Smalyukh, P. van der Schoot, and M. Pasquali, Experimental realization of crossover in shape and director field of nematic tactoids, Phys. Rev. E **91**, 042507 (2015).
[45] K. L. Weirich, K. Dasbiswas, T. A. Witten, S. Vaikuntanathan, and M. L. Gardel, Self-organizing motors divide active liquid droplets, Proc. Natl. Acad. Sci. USA **116**, 11125 (2019).
[46] Z. Lansky, M. Braun, A. Lüdecke, M. Schlierf, P. R. Ten Wolde, M. E. Janson, and S. Diez,Diffusible crosslinkers generate directed forces in microtubule networks, Cell **160**, 1159 (2015).
[47] M. Braun, Z. Lansky, G. Fink, F. Ruhnow, S. Diez, and M. E. Janson, Adaptive braking by Ase1 prevents overlapping microtubules from sliding completely apart, Nat. Cell Biol. **13**, 1259 (2011).
[48] G. H. Lai, R. Coridan, O. V. Zribi, R. Golestanian, and G. C. L. Wong, Evolution of Growth Modes for Polyelectrolyte Bundles, Phys. Rev. Lett. **98**, 187802 (2007).
[49] S. Dutta, P. Benetatos, and Y. S. Jho, Bundle formation in parallel aligned polymers with competing interactions, Europhys. Lett. **114**, 28001 (2016).
[50] G. M. Grason, Chiral and achiral mechanisms of self-limiting assembly of twisted bundles, Soft Matter **16**, 1102 (2020).
[51] M. F. Hagan and G. M. Grason, Equilibrium mechanisms of self-limiting assembly, arXiv:2007.01927 [Rev. Mod. Phys. (to be published)].
[52] M. Novak, B. Polak, J. Simunić, Z. Boban, B. Kuzmić, A. W. Thomae, I. M. Tolić, and N. Pavin, The mitotic spindle is chiral due to torques within microtubule bundles, Nat. Commun. **9**, 3571 (2018).
[53] D. J. Needleman, M. A. Ojeda-Lopez, U. Raviv, K. Ewert, J. B. Jones, H. P. Miller, L. Wilson, and C. R. Safinya, Synchrotron X-ray Diffraction Study of Microtubules Buckling and Bundling under Osmotic Stress: A Probe of Interprotofilament Interactions, Phys. Rev. Lett. **93**, 198104 (2004).
[54] D. J. Needleman, M. A. Ojeda-Lopez, U. Raviv, K. Ewert, H. P. Miller, L. Wilson, and C. R. Safinya, Radial compression of microtubules and the mechanism of action of taxol and associated proteins, Biophys. J. **89**, 3410 (2005).
[55] T. Sanchez, D. T. N. Chen, S. J. Decamp, M. Heymann, and Z. Dogic, Spontaneous motion in hierarchically assembled active matter, Nature (London) **491**, 431 (2012).
[56] T. Sanchez, D. Welch, D. Nicastro, and Z. Dogic, Cilia-like beating of active microtubule bundles, Science **333**, 456 (2011).
[57] F. J. Nédélec, T. Surrey, A. C. Maggs, and S. Leibler, Self-organization of microtubules and motors, Nature (London) **389**, 305 (1997).
[58] L. M. Lemma, S. J. DeCamp, Z. You, L. Giomi, and Z. Dogic, Statistical properties of autonomous flows in 2d active nematics, Soft Matter **15**, 3264 (2019).
[59] J. A. Cohen and S. Highsmith, An improved fit to Website osmotic pressure data, Biophys. J. **73**, 1689 (1997).
[60] T. Funami, Y. Kataoka, M. Hiroe, I. Asai, R. Takahashi, and K. Nishinari, Thermal aggregation of methylcellulose with different molecular weights, Food Hydrocolloids **21**, 46 (2007).
[61] J. Brandrup, E. H. Immergut, E. A. Grulke, A. Abe, and D. R. Bloch, *Polymer Handbook*, 4th ed. (Wiley, New York, 1989), Vol. 7.
[62] K. Devanand and J. C. Selser, Asymptotic behavior and long-range interactions in aqueous solutions of poly(ethylene oxide), Macromolecules **24**, 5943 (1991).
[63] N. Ziebacz, S. A. Wieczorek, T. Kalwarczyk, M. Fiałkowski, and R. Hołyst, Crossover regime for the diffusion of nanoparticles in polyethylene glycol solutions: Influence of the depletion layer, Soft Matter **7**, 7181 (2011).
[64] A. V. Kaznacheev, M. M. Bogdanov, and A. S. Sonin, The influence of anchoring energy on the prolate shape of tactoids in lyotropic inorganic liquid crystals, J. Exp. Theor. Phys. **97**, 1159 (2003).
[65] P. Prinsen and P. Van Der Schoot, Continuous director-field transformation of nematic tactoids, Eur. Phys. J. E **13**, 35 (2004).